Tensile Deformation Damage in SiC Reinforced Ti-15V-3Cr-3Al-3Sn

Bradley A. Lerch and James F. Saltsman
Lewis Research Center
Cleveland, Ohio

April 1991

NASA

TENSILE DEFORMATION DAMAGE IN SiC REINFORCED

Ti-15V-3Cr-3Al-3Sn

Bradley A. Lerch and James F. Saltsman
National Aeronautics and Space Administration
Lewis Research Center
Cleveland, Ohio 44135

SUMMARY

The damage mechanisms of a laminated, continuous SiC-fiber-reinforced Ti-15V-3Cr-3Al-3Sn (or Ti-15-3) composite were investigated. Specimens consisting of unidirectional as well as cross-ply laminates were pulled in tension to failure at room temperature and 427 °C and subsequently examined metallographically. Selected specimens were interrupted at various strain increments and examined to document the development of damage. When possible, a micromechanical stress analysis was performed to aid in the explanation of the observed damage. The analyses, which provided average constituent microstresses and laminate stresses and strains, revealed that the damage states are dependent on the fiber architecture.

INTRODUCTION

Metal matrix composites (MMC) are being developed for high temperature applications in the engines and in the structures of hypersonic flight vehicles. Both applications require a stiff, lightweight material capable of carrying significant thermal and mechanical loads. Conventional monolithic materials are currently operating at or near their limits and cannot meet the demands of the next generation of engines and flight vehicles.

A promising candidate material is SiC-fiber-reinforced Ti-15-3. This composite material offers the potential for meeting the above requirements but only if several new problems can be solved. The SiC fiber and the titanium matrix have significantly different mechanical and thermal properties, and it is necessary to understand how these differences affect the behavior of the composite.

The purpose of this study is to investigate the damage mechanisms produced by tensile loads at room temperature (21 °C) and at 427 °C (800 °F). The damage is determined by metallographic methods, and a micromechanical stress analysis program is used to further understand the observed damage.

EXPERIMENTAL PROCEDURE

Material

The composite material vendor fabricated the material by alternating layers of Ti-15V-3Cr-3Al-3Sn (Ti-15-3) foils and of continuous SCS-6 (SiC) fibers. The unidirectional and crossplied fiber layups were hot isostatically pressed at high temperatures using proprietary

consolidation procedures. The material consisted of eight fiber layers to yield 2-mm-thick plates with a nominal fiber volume fraction of 34 percent. Detailed descriptions of the microstructure have been given previously (ref. 1). These composite plates were manufactured in 1987 and contained a titanium wire weave which kept the SiC fibers parallel during consolidation.

Since fiber-matrix interface damage will be discussed in this report, a brief description of the as-manufactured interface is given at this time. Figure 1 shows a cross section of a portion of the SiC fiber. The SiC is deposited on a carbon core (refs. 2 and 3), and then a two-pass carbon coating is deposited on the outer surface of the fiber. This coating reacts with the matrix on consolidation to form a 0.3-μm-thick reaction zone. More details on the coating and reaction zone can be found in reference 1.

Specimen Preparation

Tensile specimens were cut from the composite plates using electrical discharge machining (EDM). Specimens were cut from one of four plates, depending on the desired fiber orientation. The $[0°]_8$ and $[90°]_8$ specimens were taken from one plate, the $[\pm45°]_{2s}$ specimens from another, the $[\pm30°]_{2s}$ and $[\pm60°]_{2s}$ specimens from a third, and the $[0°/90°]_{2s}$ and $[90°/0°]_{2s}$ specimens from the remaining plate. The first number of the standardized laminate stacking code refers to the orientation of the outermost plies. Both straight-sided and dogbone-shaped (reduced-gage-section) specimen geometries in several dimensions were tested, primarily to investigate the effects of gage width and specimen geometry on tensile properties. Specimen dimensions are given in figure 2.

Most specimens were heat treated (24 hr at 700 °C in vacuum) before testing. The purpose of this heat treatment was to partially stabilize the α-β Ti structure (ref. 4). The remainder of the specimens were tested as-received.

Tensile Tests

Specimens were pulled in tension in a servohydraulic load frame. Hydraulically actuated collets transferred the load from the grips to the specimens. Stainless-steel tabs were glued onto the ends of the specimens to add thickness and thereby maintain the proper collet pressure. The tabs were as wide as the specimen ends, were approximately 3.2 cm long, and were beveled approximately 20° at the end nearest the gage section.

Strain was measured using a 1.3 cm gage length, clip-on extensometer. The alumina probes used to contact the specimen permitted strain measurement at high temperatures. The specimens were loaded in strain control at a strain rate of 10^{-4} per sec unless otherwise indicated. Stress-strain data were recorded digitally as well as on an analog recorder.

Specimen heating was accomplished through an induction coil powered by a 5-kW RF heater. Only the 15.2-cm-long reduced-gage-section specimens were used for the high temperature tests. The temperature gradient was measured using a composite specimen that had six thermocouples spot welded onto its gage section. The temperature difference at 427 °C (800 °F) between any two thermal couples was at most 5 °C (10 °F). The temperature was controlled during the test by one thermocouple spot welded at midgage.

2

Metallography

Scanning electron microscopy (SEM) of the fracture surfaces was performed on selected specimens. Damage modes for both failed and interrupted tests were examined using optical metallographic techniques that had been developed previously for this material (ref. 1). Specimen section orientations (fig. 3) were transverse (sectioned perpendicular to the load axis), through-the-thickness (sectioned parallel to the load axis), and face (sectioned parallel to an individual ply). A sufficient number of untested sections were polished to ensure that the different types of damage were not a result of metallographic preparation. Microhardness was measured in the matrix to determine if specimen to specimen variations existed in the chemical composition. Such variations could cause differing matrix constituent properties.

RESULTS

Data from Room Temperature Tests

Typical stress-strain curves for room temperature tests are presented in figure 4 for all the fiber orientations tested as well as for the unreinforced matrix. As expected, the $[0°]_8$ layup is the strongest, followed by, in order of decreasing strength, the $[90°/0°]_{2s}$ and $[0°/90°]_{2s}$, $[\pm30°]_{2s}$, $[\pm45°]_{2s}$, $[90°]_8$, and $[\pm60°]_{2s}$ layups. Note that the $[90°/0°]_{2s}$ and $[0°/90°]_{2s}$ layup specimens have comparable mechanical properties. Also, the $[\pm60°]_{2s}$ and $[90°]_8$ layup specimens had approximately the same strength. In general, the degree of nonlinear behavior increased as the strength decreased. The tensile properties for each specimen are given in table I. The average moduli are

Material	Average initial modulus of elasticity, E_1, Gpa
Fiber	395
$[0°]_8$	185[a]
$[90°/0°]_{2s}$, $[0°/90°]_{2s}$	145
$[\pm30°]_{2s}$	145
$[90]_8$	125
$[\pm60°]_{2s}$	115
$[\pm45°]_{2s}$	115
Matrix	90

[a]Calculated without the value of specimen 5.

Specimen 5 (see table I) had a much higher modulus than the other unidirectional $[0°]_8$ specimens (i.e., 258 GPa compared with an average of 185 Gpa). Its fiber volume fraction and matrix hardness were comparable with those values for the other $[0°]_8$ specimens (table I), excluding the possibility that either might have led to the higher modulus. Metallographic evaluation, however, indicated that the reaction zone surrounding approximately half of the

fibers in this specimen was 3 μm thick (fig. 5) rather than the 0.3 μm observed in the other specimens (ref. 1). Although the cause of this large reaction zone is unknown, with all other factors equal, we conclude that the interface can significantly affect the elastic modulus of the composite.

Excluding the $[0°]_8$ orientation, all layups contained a second linear portion in the stress-strain curves. An example of this is shown in figure 6 for a $[0°/90°]_{2s}$ specimen. The slope of this second linear portion is indicated in table I as E_s. The E_s values are always significantly less than the initial modulus, E_I. The reasons for the decrease in stiffness compared with E_I will be discussed later.

The room temperature ultimate tensile strengths (UTS) are also listed in table I, and their averages are listed below in order of decreasing strength.

Material	Ultimate tensile strength, UTS, MPa
$[0°]_8$	1395
$[90°/0°]_{2s}$, $[0°/90°]_{2s}$	1020
$[\pm30°]_{2s}$	995
Matrix	870
$[\pm45°]_{2s}$	530
$[90°]8$	420
$[\pm60°]_{2s}$	390

Also listed in table I is the strain to failure, ϵ_f (i.e., the strain at complete separation) for each specimen. The average room temperature failure strain was smallest for the $[0°]_8$ orientation and equal to 0.90 percent. (Specimen 2 was not included in this average because it was erroneously loaded to 700 MPa before testing, and this loading is believed to have decreased both the UTS and failure strain. Specimen 5 was also excluded because of its anomalous microstructure). Failure strains for the $[90°]_8$, $[90°/0°]_{2s}$, $[0°/90°]_{2s}$, $[\pm30°]_{2s}$, and $[\pm60°]_{2s}$ layups were nominally the same and range from approximately 1 to 2 percent. The test of the $[\pm45°]_{2s}$ specimen was interrupted at 4 percent strain. Based on the failure strain of 7.29 percent at 427 °C, the failure strain at room temperature was expected to be between 4 and 7 percent. Because of the large specimen to specimen variation in failure strain for all orientations (except $[0°]_8$), this property will not be used for further comparisons in this report.

Fiber volume fraction was determined for selected specimens (primarily $[0°]_8$ and $[\pm30°]_{2s}$) and is given in table I. The average volume fraction was 34 percent. Within the small range of scatter in the fiber volume fraction, no correlation could be determined between it and any tensile property.

4

The heat-treatment condition of each specimen is also listed in table I. Heat treatment can change the matrix properties and thereby affect the composite properties. Although heat treatment effects were not specifically addressed in this study, both as-received and heat treated (for 24 hr at 700 °C in vacuum) specimens were tested. No difference was observed in the tensile properties (table I), which was expected since the heat treatment used produces matrix properties that are similar to those of the as-received condition (ref. 4). This can be observed by the similar hardnesses for each condition as listed in table I.

Vicker's hardness was measured for the matrix in several specimens (table I). Each value presented is an average of 10 measurements. The range of the hardness values per specimen was approximately ± 10 H_V. Within the range of heat treatment conditions used, all specimens had the same matrix hardness. This would not necessarily be the case for other heat treatments (ref. 4). No correlation could be determined between tensile properties and the limited variation in matrix hardness.

The $0°/90°$-strain gage rosettes were mounted on a few of the $[0°]_8$, $[90°]_8$, and $[90°/0°]_{2s}$ specimens such that strains parallel and perpendicular to the load axis were measured. The purpose was twofold: (1) to verify the strain readings from the edge-mounted extensometer and (2) to measure the transverse strain allowing the calculation of Poisson's ratio, ν_{12}. Figure 7 compares the stress-strain response for both the extensometer and the longitudinal strain gage. Good agreement is observed between the two measurements. The stress-strain curves from the transverse direction have also been plotted in these figures. The stress-transverse strain curve for the $[0°]_8$ specimen (fig. 7(a)) has a nonlinear portion that begins at a stress of approximately 900 MPa, the same as in the longitudinal strain curve. Both transverse and longitudinal strain curves for the $[90°]_8$ and $[90°/0°]_{2s}$ (fig. 7(b) and (c)) specimens show bilinear behavior at low strains. The change in slopes occurs at approximately 275 and 180 MPa for the $[90°]_8$ and $[90°/0°]_{2s}$ specimens, respectively.

The specimens $[90°/0°]_{2s}$ (fig. 7(c)) exhibited a unique behavior in the transverse direction. At approximately 700 MPa transverse stiffness increased, as seen by the upward turn in the stress-strain curve and this change corresponded to the large nonlinearity observed in the longitudinal direction. This behavior was reproduced on a second $[90°/0°]_{2s}$ specimen. The reason for this behavior is currently under investigation.

Poisson's ratios were calculated for each orientation and are as follows:

Material	Poisson's ratio, ν_{12}
$[0°]_8$	0.28
$[90°/0°]_{2s}$	0.21, 0.15
$[90°]_8$	0.17

The large variation in the Poisson's ratio for the $[90°/0°]$2s specimens (specimens C4 and C5) is a manifestation of the lower modulus from specimen C5. The value of 0.21 lies between the values for the $[0°]_8$ and $[90°]_8$ specimens and is therefore believed to be more representative of the $[90°/0°]_{2s}$ specimens. The lower value of 0.15 and the low modulus of specimen C5 will be discussed later in this report.

5

During testing of some specimens, discontinuous stress-strain behavior was observed (fig. 8). At the lower strains, the sudden load drop was accompanied by an audible click. This behavior was observed primarily at room temperature for some of the $[0°]_8$ and $[\pm30°]_{2s}$ layups that were tested as 10.2-cm (4-in.) long samples. We do not know why the shorter specimen length was more prone to this behavior. Metallographic examination of these specimens from tests which were continued to failure, and of specimens from tests interrupted after the load drop failed to reveal the cause for this behavior.

Other discontinuities in the tensile curves were occasionally observed near final fracture (fig. 8, $[\pm30°]_{2s}$ curve). This behavior was only observed in room temperature tests for the $[\pm30°]_{2s}$ specimens. Its cause is unknown but is believed to be due to the propagation and arrest of cracks.

Data from 427 °C Tests

Typical stress-strain behavior for $[0°]_8$ and $[90°]_8$ specimens tested at 427 °C are shown in figure 9. Also presented in this figure are typical room- temperature data for the same orientations. Within the scatter of specimen-to-specimen variation, there is no detectable influence of temperature on the tensile behavior. This can also be observed by comparing the tensile properties at room temperature and 427 °C for these two orientations (table I). However, there is a difference in the tensile behavior between room temperature and 427 °C for the $[\pm45°]_{2s}$ and $[\pm60°]_{2s}$ layups (fig. 10 and table I). Test specimens of these two layups are less stiff and weaker at 427 °C than the ones tested at room temperature. Tangent moduli at selected stress levels, corresponding to E_I and E_s, are listed in table I and shown in figure 10.

Specimens having $[0°]_8$, $[90°]_8$, and $[\pm45°]_{2s}$ layups were tested at 427 °C at different strain rates. The $[0°]_8$ specimens were pulled at 10^{-3}, 10^{-4}, and 10^{-5} sec^{-1}, (see fig. 11). No strain rate effects were observed. Likewise, the $[90°]_8$ specimens showed no strain rate effects for the order of magnitude change in strain rate examined (fig. 12). The stress-strain curves for the $[\pm45°]_{2s}$ specimens showed similar tensile properties for both strain rates used (fig. 13). However, the waviness of the stress-strain curve for the specimen tested at the slower rate indicates that some rate dependent behavior may be present. The cause of this waviness is believed to be actual material behavior (as will be shown later) and not an artifact of the test.

Fractography

The location of the primary crack (i.e., the crack leading to failure) was recorded for each specimen and is listed in table I. Most of the specimens failed in the gage section. Those specimens which broke between the extensometer probes are indicated as "mid-gage" failures and those that broke in the transition between the radius and the gage section are termed "radius" failures. All other failures occurred in the gage section (this was 3.8-cm long for most specimens), but outside the extensometer probes, and these are termed "gage" failures. All of the 10.2-cm-long straight-sided specimens failed in the grip area under the tab. The longer straight-sided specimens failed in the gage. There was no noticeable correlation between any tensile property and the location of failure.

The macroscopic crack plane varied as a function of fiber orientation (fig. 14(a)). The $[0°]_8$, $[0°/90°]_{2s}$, and $[90°/0°]_{2s}$ specimens cracked on a plane approximately perpendicular to

the load axis with minimal steps or jogs. The cracking was independent of the test temperature and strain rate. For the $[90°]_8$ specimens the crack plane was also perpendicular to the loading axis and was generally very smooth. This was, again, independent of the test conditions. The cracks in the $[\pm30°]_{2s}$ specimens (fig. 14) took an irregular path, being at some places perpendicular to the load axis, and others at approximately 65° to the load axis. The proportion of these two crack paths varied from specimen to specimen. Cracks in the $[\pm60°]_{2s}$ specimens (fig. 14) followed one set of fibers, causing the specimen to break smoothly at a 60° angle to the load axis. The only $[\pm45°]_{2s}$ specimen tested to failure (due to their high ductilities) was specimen A6 (tested at 427 °C). This specimen contained a "V"-shaped crack (fig. 14), with one surface being ≈65° and the other ≈55° to the load axis. This was the only specimen that had a significant reduction in area.

We shall now discuss in detail the fracture characteristics for each layup.

$[0°]_8$ Layups. - The fracture surfaces obtained during both room temperature and 427 °C were macroscopically flat. The fiber pullout observed left fibers extending out of the matrix for maximum distances of one to two fiber diameters (fiber diam = 145 μm). Delamination occurred in some fiber rows (fig. 15(a)) and in some rows extended across the entire specimen width. Delamination was most prevalent where the fibers were closely spaced. The matrix debonded from the fibers in most areas and contained shear lips which had formed immediately adjacent to the fibers (fig. 15(b)). The largest gaps between the matrix and the fiber were between fiber rows rather than between fibers within a row. The remainder of the matrix failed by tensile overload as indicated by microvoid coalescence (fig. 15(a) and (b)). At 427 °C the matrix flowed more readily as indicated by the necking of the matrix surrounding each fiber (fig. 15(c)). The matrix even necked between fibers within a fiber row, which was not observed at room temperature. The amount of delamination appears to be less at 427 °C although more tests are needed to confirm this.

$[90°]_8$ Layups. - Cracking in this fiber layup occurred parallel to the fibers, forming a flat fracture surface (fig. 16). Occasionally, sections of matrix and/or composite were ripped off in chunks. The fibers were either intact or completely missing, and no fiber splitting was observed. If fibers were missing, a groove remained where the fiber once was. The matrix failed similarly to that in the $[0°]_8$ specimens in that shear lips formed next to the fibers and microvoid coalescence occurred elsewhere (fig. 17(a)). At 427 °C cleavage was an important matrix cracking mechanism as depicted in figure 17(b). More necking of the matrix surrounding the fibers was also observed at 427 °C.

$[0°/90°]_{2s}$ and $[90°/0°]_{2s}$ Layups. - The $[0°/90°]_{2s}$ and $[90°/0°]_{2s}$ specimens behaved similarly and will therefore be discussed together. These specimens' fracture surfaces were identical to the $[0°]_8$ or $[90°]_8$ specimen fractures for those plies oriented at 0° or 90°, respectively, to the load axis. The overall fracture surfaces showed evidence of fiber pullout (fig. 18) in the 0°-plies, and missing fibers or fiber-matrix separation in the 90°-plies. The matrix failed through tensile overload as evidenced by microvoid coalescence and shear lips next to the fibers (fig. 19). Some delamination was observed in the 0° plies.

$[\pm30°]_{2s}, [\pm45°]_{2s}, [\pm60°]_{2s}$ Layups. - Examination of these fracture surfaces revealed relatively little additional information. In general, microvoid coalescence and shear lips were observed in the matrix. More matrix ductility was observed at 427 °C, as indicated by increased amounts of necking. Also, some cleavage failure was observed at the high temperature. As the fiber angle increased with relationship to the load axis, larger lengths of

fibers were observed protruding from the fracture (fig. 20(a) to (c)). This is not to say that the fiber pullout length increased, but rather that certain plies were oriented such that they behaved similar to the $[90°]_8$ specimens wherein long lengths of fibers (or grooves) debonded from the matrix. Also, the fracture surfaces resembled the $[0°]_8$ specimens at the lower fiber angles (i.e., $[\pm30°]_{2s}$) and approached the appearance of the $[0°/90°]_{2s}$ specimens as the angle increased (i.e., $[\pm45°]_{2s}$ or $[\pm60°]_{2s}$).

Optical Microscopy of Specimens Tested to Failure

In this section, only failed specimens are discussed. Tests that were interrupted before failure are discussed in a later section.

$[0°]_8$ Layups. - Specimens tested to failure at room temperature exhibited extensive fiber cracking and debonding near the fracture surface (fig. 21). These cracks were generally perpendicular to the fiber axis. Away from the fracture surface, few cracks, if any, were observed. Figure 21 also shows a group of secondary fiber cracks in the second ply, ≈5 mm below the fracture surface. These cracks occurred in the area of a titanium wire and are better observed in the etched specimen of figure 22(a). This row of fiber cracks was not observed in the first ply, since the titanium wire did not appear there.

Debonding of the interface can also be observed in the area of the titanium wire. Debonding occurred between the fiber and the reaction zone (i.e., in the carbon coating, see fig. 1), leaving the reaction zone adhering to the matrix. This was always the case, regardless of ply orientation, and therefore, no further differentiation will be made as to where (i.e., in which portion of the carbon-coating) debonding occurred since this was dependent on the specific fiber and not on fiber orientation and test condition. Extensive debonding was observed near the fracture surface, with much less fracture occurring at locations farther away from the fracture surface. Some debonding was observed near the fiber cracks, and some was noticed in areas where the fibers were not cracked.

Other than the primary crack (which led to failure), no other matrix cracks were observed. The exceptions were those cracks which sometimes occurred in the matrix in the area of a titanium wire. An example of this is shown in figure 22(b), which is from the same general area of the sample in figure 22(a), but, here, the sample is unetched to permit viewing of the matrix cracks. These cracks were small and rarely propagated to the next fiber.

Examination of specimens tested at 427 °C showed an increase in matrix ductility at this temperature as evidenced by matrix necking on the fracture surface (fig. 23). This behavior was not observed in specimens tested at room temperature (compare with figs. 21 and 23). The specimens tested at 427 °C also showed extensive fiber cracking and debonding near the fracture surface and little or no matrix cracking. More fiber cracks were observed away from the fracture surface but these cracks could have been due to specimen to specimen variations and not necessarily to test temperature. One unique observation from the 427 °C test is shown in figure 24. In the through-the-thickness section shown the specimen has necked at the fracture surface. As a result fibers cracked extensively, and the fibers in the outer most plies bent toward the center of the specimen. This necking was not observed in the width nor in any orientation tested at room temperature.

[90°]$_8$ Layups. - Examination of the fracture surfaces showed no difference between those specimens tested at room temperature and those at 427 °C. Other than the primary crack, few matrix cracks, if any, were observed. Figure 25 is a through-the-thickness section showing matrix cracks emanating radially from a debonded fiber. Most fibers were debonded in these specimens. Examination of the first fiber row (fig. 26) shows extensive fiber cracking and splitting only near the fracture surface, which suggests that there was some bending moment, perhaps due to the final fracture.

[0°/90°]$_{2s}$ Layups. - No differences were observed between the [0°/90°]$_{2s}$ and the [90°/0°]$_{2s}$ specimens. The observations from optical microscopy will be presented in terms of 0° and 90° plies.

The 90° plies exhibited deformation similar to the unidirectional, [90°]$_8$ specimens. Fiber cracks and splitting were observed near the fracture surface and at the edges of the specimen. Debonding was also observed along most fibers. The 0° plies contained extensive fiber cracking near the fracture surface. However, unlike the unidirectional [0°]$_8$ specimens, the 0° plies in this layup also contained fiber cracks remote from the fracture surface (fig. 27). These cracks were not randomly spaced, but were located in groups perpendicular to the fiber axis. As with the 90° plies, few matrix cracks were observed, even in areas which contained fiber cracks. Debonding was also observed in the 0° plies and to a much greater extent than was seen in the unidirectional [0°]$_8$ material.

[±30°]$_{2s}$ Layups. - The fracture profile in the first ply is shown in figure 28(a). The fibers, as well as the matrix slivers between the fibers, have rotated as if to align themselves with the load axis. Extensive fiber cracking occurred near the fracture surface, with less occurring away from it. Fiber cracks initiated on one side of the fiber (fig. 28(b)). Some of these cracks did not propagate completely across the fiber diameter. Debonding was also observed along most fibers. Matrix cracks were rarely observed, except when associated with a leach pit, as depicted in figure 29. These pits were observed frequently on the crossplied material and reportedly result from the manufacturing process. The hot isostatic press (HIP) can after consolidation is removed using an acid solution. If not done correctly, the solution can etch the composite matrix leaving a pit (fig. 29). In this study these pits usually acted as crack initiators, regardless of fiber orientation. Since there is no way to assess their effect on the mechanical behavior, although it probably degrades properties, they will not be further discussed. It is interesting to note however, that cracks initiating at the tip of a leach pit were always arrested at the first fiber row.

[±60°]$_{2s}$ Layups. - Optical microscopy investigations revealed no differences between specimens tested at room temperature and at 427 °C. The primary fracture followed one set of fibers, and in these plies the damage was similar to that seen in unidirectional, [90°]$_8$ specimens. Few, if any, matrix cracks were observed. Some fiber cracks perpendicular to the fiber axis were observed, but no longitudinal splitting at the specimen edges was seen, as was the case in the unidirectional, [90°]$_8$ specimens. Debonding was observed along nearly every fiber. Figure 30 shows a through-the-thickness section showing a debonded fiber. The gap between the interface and the fiber is largest on the ends that are nearly parallel to the thickness of the specimen. The other sides of the fiber, that is those that are parallel to the length of the specimen, contain radial coating cracks, some of which extend into the reaction zone.

Although the fracture followed one set of fibers, the other set (i.e., the crossplies) were fractured in a manner similar to that of the [±30°]$_{2s}$ specimens. Figure 31 shows extensive

9

bending of the fibers and matrix toward the loading axis. Fiber cracks occurred throughout the specimen, and propagated perpendicular to the fiber axis. Near the fracture surface, fiber damage is extensive. Again, nearly every fiber was debonded.

$[\pm45°]_{2s}$ Layups. - This orientation contained unique damage modes. Testing of the room temperature specimen was stopped at 4 percent strain. Extensive fiber cracking and debonding had occurred. The fiber cracks were perpendicular to the fiber axis. Some matrix cracking was observed in through-the-thickness sections (fig. 32), and these cracks appeared to initiate on the face. No matrix cracks were observed beyond the first fiber row.

The specimens tested at 427 °C sustained a large amount of damage. Fibers were extensively cracked, even in areas far removed from the fracture surface (fig. 33). The fiber cracks were not always perpendicular to the fiber axis but were bent, approaching a longitudinal direction. Large gaps associated with debonding were also seen. Extensive matrix cracking is also observed in figure 33. The matrix in several areas has necked down and resulted, in some areas, in a 43-percent reduction in area. Figure 34 shows the edge of the specimen at which the matrix has been stretched past the plane of the fiber ends by approximately one fiber diameter. This figure also shows a waviness in the fibers and matrix slivers between fibers which is due to the large amounts of damage.

Testing at a slower strain rate of 10^{-5} sec^{-1} at 427 °C resulted in observable slip bands in the matrix (fig. 35). Slip could not be resolved in any of the other tested specimens. It is believed that the appearance of these bands is a dynamic strain aging effect caused by the slower straining rates. Thus, the waviness in the stress-strain curve observed in figure 13 is believed to be a consequence of dynamic strain aging.

Optical Microscopy of Specimens From Interrupted Tests

Damage development and the cause of nonlinearities in the stress-strain curve was investigated using interrupted tests. Specimens were pulled to various points in the stress-strain curve and then examined metallographically for cracking, debonding, and evidence of matrix flow.

$[0°]_8$ Layups. - A specimen was interrupted at a longitudinal strain of 0.5 percent which represents the first signs of nonlinearity (point A in fig. 7(a)). No damage was observed in the composite. A second specimen was strained just short of failure (point B in fig. 7(a)) to a longitudinal strain of 0.85 percent. This strain is 94 percent of the average failure strain of 0.90 percent for the $[0°]_8$ orientation. No matrix or fiber cracks were observed, nor was there any evidence of delamination. However, some debonding was evident (fig. 36).

$[90°]_8$ Layups. - One specimen was tested to a strain of 0.6 percent (point A in fig. 7(b)) which is in the nonlinear portion of the stress-strain curve. The only damage observed was some limited debonding of the fibers. A specimen tested to a higher strain of 1.0 percent (point B in fig. 7(b)), suffered extensive debonding, as indicated by the larger interfacial gaps and the increase in the number of fibers debonded (fig. 37). No fiber or matrix cracking was observed.

$[30°]_{2s}$ Layups. - A specimen was strained to 0.8 percent, well into the nonlinear range (see point A in fig. 38). Examination of this specimen showed considerable debonding as indicated in figure 39. In some areas of debonding, the matrix slivers between fibers had begun to neck.

Some matrix cracks were observed, but these were limited to the outer matrix sheet and were always associated with the leach pits (fig. 29). There was also one isolated area in which cracks (a total of five cracks) were found in four fibers. This area was on the edge of the specimen and in the second ply. No other fiber cracks were observed.

DISCUSSION

Specimen design is a concern for testing composite materials. If the specimen width is too narrow, sufficient constraint may not be present to use the fibers effectively. This would especially apply to off-axis or transverse orientations. Polymeric matrix composites have typically been tested in large forms (ref. 5), but the cost and material usage is prohibitive for the MMC's. There is also some debate on the issue of straight-sided versus reduced-gage-section specimens. The reduced- gage-section specimens often crack in the radius or split from the radius into the tab area. Straight-sided specimens have the disadvantage that the gage length is undefined, which could present problems in high temperatures testing where temperature uniformity is important. These issues have been addressed, to some extent, in this study.

Straight-sided and reduced-gage-section specimens were tested in tension for various layups and at room temperature. The following discussion applies to $[0°]_8$ and $[\pm30°]_{2s}$ layup specimens room temperature since there was a large enough sample for these tests. Results from tests on other layups did not contradict these conclusions. As can be observed in table I, no difference in tensile properties was observed between straight-sided or reduced-gaged-section specimens. Some of the reduced-gage-section specimens did break in the radius, but this was found to have no influence on the tensile properties. The straight-sided, 10.2-cm-long specimens all failed in the tab region. A nonlinear finite-element analysis has indicated that a stress concentration was located under the tabs (ref. 6). This stress concentration resulted from the clamping forces of the grips. The specimen and tab length, as well as the nonlinear behavior of the composite and tab material, influence the magnitude of this stress concentration. By increasing the length of the specimen and tabs or by reducing the gage section, the specimen fails before the stresses under the tabs become large enough to induce cracking.

Another disadvantage of the 10.2-cm-long specimens is that they are prone to sudden load drops (fig. 8). It is possible that these load drops, and the audible click associated with them, were caused by partial debonding of the tab from the specimen. This debonding may have been induced by the stress concentration in the tab region.

In order to investigate gage width effects, $[\pm30°]_{2s}$ straight-sided and reduced-gage-section specimens having different widths were pulled in tension at room temperature. Gage widths of 0.75, 1.25, 1.90, and 2.55 cm were used. These specimens exhibited identical tensile properties (see table 1), indicating that the specimen geometries generally used for MMC's are adequate. One interesting effect of specimen geometry was observed in $[\pm30°]_{2s}$, large dogbone specimens (geometry G in fig. 2). In these specimens, the gage width was 1.90 cm, and the gage length was only 1.25 cm. Thus, the fiber orientation was such that fibers that began in the straight portion of the gage ended in either the radius or in the wide, tab area of the specimens. No fibers both began and ended in the gage section. This provided additional constraints to the specimen and these specimens had UTS and failure strain values in the upper and lower ends, respectively, of the $[\pm30°]_{2s}$ specimen data. Thus, care should be taken to ensure that enough fibers are completely contained in the gage section. This becomes an important issue and would necessitate longer specimens for layups containing fibers at very shallow angles, e.g. $[\pm15°]$.

11

Fiber volume fraction could also affect the composite properties, especially since constituent volume fraction enters into the micromechanics equations. However, no large variation in fiber volume fraction was detected (table I), and the small specimen to specimen variations in fiber volume fraction could not be correlated with any tensile property. In fact, the only microstructural observation that significantly affected the properties was the enlarged reaction zone in specimen 5 (fig. 5). Since the interface in this material is weak (ref. 7), the large reaction zone may have allowed for stronger fiber matrix bonding in this specimen. Even so, a rule-of-mixtures calculation, which assumes perfect bonding, only gives a composite modulus of 195 GPa, which was observed in most $[0°]_8$ tests. Specimen 5 had a modulus of 260 GPa. This value cannot be obtained by considering a higher modulus interface as a third constituent because the volume fraction of the reaction zone is too small. Naik et al. (ref. 8) have reported that an increase in modulus could be obtained by a superplastic diffusion bonding cycle, which reacted the matrix with the carbon-coating, thus eliminating the layered interface. They reported a change of 9 percent in modulus, which is much lower than the change observed in specimen 5. This issue should be further pursued, since interface control could be a viable method to enhance the stiffness of the composite.

In order to better understand the relationship between the stress-strain curves and the observed damage mechanisms, the composite stress-strain behavior was modeled using the laminate program AGLPLY (ref. 9). This code is based on the fiber vanishing diameter model (ref. 9) and incorporates the elastic-plastic response of the matrix. The fiber was assumed to be elastic. Laminate behavior as well as average constituent microstresses can be described. The input values used for the constituents are given in the appendix along with an estimate of residual stresses induced during consolidation.

The predicted laminate stress-longitudinal strain curve is given for the $[0°]_8$ layup in figure 45 along with the experimental results from two specimens. Also included in this figure is the stress-transverse strain response. Figure 40 indicates good agreement between the predicted and experimental curves, especially for the longitudinal strain. The AGLPLY calculations for the $[0°]_8$ layup are linear to a laminate stress of ≈900 MPa. The matrix stress at this point is ≈710 MPa and corresponds to the proportional limit of the matrix (see appendix). Thus, the deviation from linearity at a laminate stress of approximately 900 MPa is predicted based on yielding of the matrix. The stress-transverse strain also indicates this point of yielding. However, no metallographic evidence of slip bands indicating matrix plasticity could be found. Even in the unreinforced matrix, which was pulled in tension producing large amounts of plasticity, no slip bands were observed.

Because the matrix has very limited strain hardening capabilities, microhardness indentations were also ineffective in determining whether plasticity occurred and caused the nonlinearity. It is not known if the debonding observed in figure 36 is sufficient to cause such nonlinearities. The only conclusive statement that can be made about the nonlinearity in the $[0°]_8$ specimens is that it is not caused by fiber cracks. It should also be pointed out that the delamination observed at failure (fig. 15(a)) was a result of the final fracture since, it was not observed in the interrupted tests nor in completed tests at locations remote from the fracture surface.

The $[0°]_8$ specimens show little evidence of damage up to nearly the failure point. The only observable change due to straining is some debonding. A quantitative measure of debonding is impossible (regardless of the fiber layup) since

12

(1) This is observed as a line defect and there is a resolution problem when the interfacial gap is small. This also inhibits defining when (i.e., at what strain) debonding starts.

(2) The interface does not debond completely, but only separates along certain portions of the fiber length and circumference, which depends on the local bond strengths and stresses. Nevertheless, large interfacial gaps can be identified in both transverse and longitudinal sections.

Predictions for the $[90°]_8$ data are shown in figure 41. The predicted and experimental data agreed in the elastic region in both the longitudinal and transverse directions. However, as the composite continued to strain, a break in the experimental stress-strain curve appeared and represents the point at which the modulus changes from E_I to E_s. This occurred at a laminate stress of ≈ 275 MPa. This initial break from linear elastic behavior has been identified by others (ref. 7), at least on the edge of the specimen, as being a result of interfacial debonding.

Metallographic investigations of the specimen interrupted at point A (fig. 7(b)) show debonded interfaces in the interior of the specimen. The debonding results in a linear region which has been denoted in this report as E_s. At the point of debonding, the input data to AGLPLY were adjusted to simulate the interfacial debonding by reducing the fiber modulus to 13 GPa which is 3 percent of its original value. The reduced modulus, E_s, was obtained by fitting the stress-longitudinal strain test data for the $[90°]_8$ orientation. This same fiber modulus was used for all other orientations when debonding was suspected.

Note that debonding does not cause a hole in the matrix (i.e., modulus of elasticity of the fiber, $E_f = 0$) since the debonding process occurs, at least initially, on only two sides of the fiber (see for example fig. 30). Therefore, in the through-the-thickness direction, the interface is still bonded. On the through-the-thickness sides, the large strains are often accommodated by cracks in the carbon-coating or reaction zone as seen in figure 30. Unfortunately, AGLPLY can only treat the fiber as orthotropic and the correct debonding process cannot be properly modeled.

It should be pointed out that after the cool down to room temperature from the heat treatment temperature of 700 °C (1290 °F), which was the assumed stress free state in the composite, AGLPLY predicted, for the unidirectional material, residual matrix and fiber stresses only in the fiber direction. All other stresses were zero. The fiber vanishing model, on which AGLPLY is based, assumes that the fibers do not influence the deformation in the transverse directions (ref. 10). Thus, only axial residual stresses are nonzero. This shortcoming of AGLPLY may also be why the stress-transverse strain predictions do not agree with the experimental data.

The residual stress calculations for all fiber orientations studied in this report are summarized in the appendix. A calculation of the residual stresses for the same set of cooling conditions was also performed for the unidirectional case using a concentric cylinder model (ref. 11). This calculation showed that a residual radial stress existed in the matrix and was compressive and equal to 90 MPa.

Experimental data for the $[90°]_8$ specimens indicate that debonding occurs at a laminate stress of 275 MPa. Note that for this layup and before debonding, the matrix and fiber stresses are both equal to the composite stress. Since the first 90 MPa of the laminate stress of 275 MPa is required to overcome the residual compressive stress at the interface, the resultant interface strength is 185 MPa.

In the nonlinear portions of the stress-strain curve, AGLPLY failed to predict the stress-strain curve as illustrated in fig. 41. Continued loading in AGLPLY up to the failure stress showed no deviation from the linear E_8 line for the longitudinal stress-strain case. This indicates that the stresses in the matrix were lower than the proportional limit. After straining to 1.0 percent (point B in fig. 7(b)), the only damage which can be observed was debonding (fig. 37). These results indicate that global plasticity in the matrix is unlikely. Similar to the $[0°]_8$ behavior, it is not known if debonding alone can account for all the nonlinearity in the curve.

The AGLPLY predictions for the $[0°/90°]_{2s}$ orientations are given in figure 42. Excellent agreement between experimental data and the calculations is observed in the longitudinal direction. For this orientation, a reduced fiber modulus only for the 90° plies was used when the radial or matrix stress in these plies reached 275 MPa. This occurred at an applied laminate stress of 180 MPa. The applied stress at which debonding occurs is lower than in the $[90°]_8$ specimens, and this is due to the effects of the 0° plies in the $[0°/90°]_{2s}$ layup. The reduced fiber modulus provided excellent agreement with the break in the elastic line as well as in the longitudinal E_8 value observed from the experiment. The predicted stress-transverse strain curve did not agree with the data except in the linear elastic region. Again, the predicted transverse E_8 was lower than the actual value and could be a result of the directional nature of debonding.

The modulus values, E_I, for the $[90°/0°]_{2s}$ layup and the identical $[0°/90°]_{2s}$ layup exhibit about 78 percent more scatter than the $[0°]_8$ layup (see table I). This scatter could not be explained by microstructural differences such as fiber volume fraction or matrix hardness. Using AGLPLY, the residual stresses due to cool down from the heat treatment temperature were calculated, and this showed that the $[90°/0°]_{2s}$ orientation had residual radial stresses in the matrix of 137 MPa. This is half of the 275 MPa necessary to debond the interface and is the largest of all layups investigated. It is conceivable that the 135 MPa residual stress is sufficiently high to cause debonding of some of the weaker interfaces, assuming that the interfaces have some statistical variation in strength.

Debonding of some interfaces would lower the modulus. It is believed that the specimens having a lower modulus had more interface debonding than those having a higher modulus. For example, the modulus of specimen C5 ($[90°/0°]_{2s}$) was 103 GPa and was lower than the E_8 value of 121 GPa for specimen C4, indicating that most of the fibers in the 90° plies were debonded. Specimen C5 also yielded a low poisson's ratio of 0.15 compared with a value of 0.21 for specimen C4.

The lower modulus of specimen A6 ($[\pm45°]_{2s}$) suggests that some of its interfaces were debonded. This suspected debonding led to difficulty in determining the value for E_8 since the stress-strain curve for some of the cross-plied laminates contained either no linear portion (i.e., the interfaces continually debonded during the test) or a very small linear portion. The $[\pm30°]_{2s}$ and $[\pm60°]_{2s}$ layups had residual radial stresses in the matrix of 95 MPa. This was lower than that of the $[90°/0°]_{2s}$ orientations, and the modulus scatter in these specimens was less than in the $[90°/0°]_{2s}$ layups.

Although no interrupted tests were performed on the $[0°/90°]_{2s}$ or $[90°/0°]_{2s}$ orientations, some conclusions can be reached by comparing the behavior of the 0° and 90° plies with the behavior of the $[0°]_8$ and $[90°]_8$ layups. The 90° plies are believed to behave similarly to the $[90°]_8$ layups, since, at failure, the 90° plies have, as the only apparent damage, interfacial

debonding (excluding the main crack). At high strains the predicted response compares adequately with the data, as shown in figure 42. The prediction is better than that of the $[90°]_8$ orientation (fig. 41) and worse than that of the $[0°]_8$ orientation (fig. 40).

For both the $[0°/90°]_{2s}$ and $[0°]_8$ orientation, the predicted nonlinearity at high strains is accounted for by matrix plasticity only. For the $[0°/90°]_{2s}$ orientation, this does not cause a large enough bend in the stress-strain curve-probably because in the $[0°/90°]_{2s}$ orientations, the 0° fibers experienced cracking (fig. 27) that could not be taken into account in the analysis. This is a different condition from the $[0°]_8$ specimen in which no cracking was observed. AGLPLY does predict a slightly higher stress at failure for the 0° fibers in the $[0°/90°]_{2s}$ than for those in the $[0°]_8$ layup. Also, the 0° fibers in the $[0°/90°]_{2s}$ layup have a small tensile load in the radial direction (see residual stress values in the appendix), while there is none in the $[0°]_8$ layup. These factors could account for the additional debonding and fiber cracks in the 0° plies of the $[0°/90°]_{2s}$ layup.

The $[\pm45°]_{2s}$ layup has a unique stress-strain response in that the failure strains are significantly larger than any of the other layups (≈7 percent compared with ≈1 percent). Prediction of the $[\pm45°]_{2s}$ stress-strain curve is shown in figure 43. There is good agreement between the predicted and experimental laminate stress and longitudinal strain in the linear elastic region. However, the predicted laminate stress at which debonding occurs is too high. Examination of the calculated matrix stresses at the point of actual debonding (250 MPa) indicates that the matrix stresses, σ_{33} and σ_{13} are 240 and 124 MPa, respectively. Since σ_{13} is a large percentage of σ_{33}, it was assumed that the shear stress would also play a role in the debonding process. Therefore, an arbitrary effective stress criterion for debonding was used in which $(\sigma_{33}^2 + \sigma_{13}^2)^{1/2} = 275$ MPa. Attainment of this criterion for the $[\pm45°]_{2s}$ specimen occurred at a predicted applied stress of 250 MPa, which agrees with the actual break in the stress-strain curve. After debonding occurred, the reduced effective fiber modulus of 13 GPa (the same value used for the $[90°]_8$ experiment) was used to calculate a value for E_s of 34 GPa, which was identical to the experimental value (table I). Again, AGLPLY cannot predict the remainder of the stress-strain curve. This is probably due to the extensive fiber cracking (fig. 33) observed at larger strains. Matrix cracking could also play a role in the nonlinear behavior.

The behavior of the $[\pm30°]_{2s}$ orientation can not be predicted using AGLPLY (as seen from figure 44). Although the linear elastic line can be accurately predicted, the rest of the stress-strain curve cannot. Using the combined stress criterion to predict debonding, the first point of nonlinearity can be adequately modeled. However, the predicted E_s slope is much lower than the experimental value. AGLPLY also predicts matrix yielding at an applied stress of 570 MPa, causing a gross overestimation of the laminate strain. A closer prediction is obtained by assuming that no debonding occurs, although the details of the experimental data are not captured, and it is clear that debonding does occur (fig. 39). The nonlinearity at high strains could be a result of local plasticity as a consequence of debonding as observed by the necking of the matrix in figure 39. Global plasticity, surface cracks from the leach pits (fig. 29), or a combination of these mechanisms could also contribute to the nonlinearity. It is unlikely that fiber cracking contributed to the nonlinearity since few fiber cracks were observed at strains less than 1 percent.

At high temperatures, the matrix softens and sheds load to the fiber. The resulting higher longitudinal stress in the fiber for the $[0°]_8$ layup could explain the increased fiber cracking at

high temperatures (compare figs. 23 and 21). The softening of the matrix also led to necking of the matrix between fibers at the fracture surface (fig. 23). The stress-strain curve at 427 °C for the $[0°]_8$ was the same as at room temperature. Prediction of the behavior using AGLPLY gave a similar curve.

Of the layups tested at both room temperature and 427 °C, only the $[\pm45°]_{2s}$ (fig. 10) and $[\pm60°]_{2s}$ had significantly different stress-strain curves. At 427 °C these layups had lower moduli. Although these moduli were predicted by ANGPLY, the point of debonding was not accurately modeled at 427 °C using the combined stress criterion.

SUMMARY OF RESULTS

SiC/Ti-15-3 laminated composites were pulled in tension at room temperature and 427 °C (800 °F). Laminate orientations tested were $[0°]_8$, $[90°]_8$, $[0°/90°]_{2s}$, $[90°/0°]_{2s}$, $[\pm30°]_{2s}$, $[\pm45°]_{2s}$, and $[\pm60°]_{2s}$. Various specimen geometries were tested to determine their effect on tensile properties. After testing, detailed fractography and metallography were performed to identify the failure modes. Tests which were interrupted before failure allowed damage development to be followed. A laminate analysis was used to determine the constituent microstresses during straining. These analyses, coupled with the metallographic observations allowed a description of the tensile behavior of the various laminates. A summary of the results are highlighted below.

(1) Both straight-sided and reduced-gage-section specimens were tested. Neither specimen design nor failure location influenced tensile properties.

(2) The 10.2-cm-long, straight-sided specimens were used only at room temperature. They broke consistently underneath the tabs and produced discontinuities in the stress-strain curve.

(3) Room temperature stress-strain curves revealed that the $[0°]_8$ layup is the strongest, followed, in order of decreasing strength, by the $[0°/90°]_{2s}$, $[\pm30°]_{2s}$, $[\pm45°]_{2s}$, $[90°]_8$, and $[\pm60°]_{2s}$ layups. In general, the degree of nonlinear behavior increased as strength decreased.

(4) The $[0°]_8$ layup showed little fiber-matrix debonding before failure. Other than the primary crack, no fiber or matrix cracks were observed in failed specimens. The nonlinearity in the stress-strain curve was predicted analytically through matrix plasticity. However, no metallographic evidence of plastic flow was observed.

(5) Damage in the $[90°]_8$ orientation was due to fiber-matrix debonding up to strains of at least 1 percent (well into the nonlinear region). This behavior is consistent with that of fractured specimens in which few secondary fiber or matrix cracks were observed.

(6) Debonding in the 90° plies of the $[0°/90°]_{2s}$ laminates led to nonlinearities in the stress-strain curves at lower strains. At higher strains, matrix plasticity was predicted, but could not be experimentally confirmed.

(7) The large scatter in the elastic moduli for $[0°/90°]_{2s}$ specimens is due to the partially debonded interfaces in pretested specimens as a result of the high residual radial stresses acting on the fiber-matrix interface.

(8) The point of fiber-matrix debonding in the $[\pm45°]_{2s}$ and $[\pm30°]_{2s}$ layups was accurately predicted using an effective arbitrary stress criterion in which both the average shear stress and radial stress in the matrix acted to separate the interface.

(9) Because of the large failure strains, the damage in the $[\pm45°]_{2s}$ specimens consisted of fiber-matrix debonding, matrix and fiber cracking, necking of matrix slivers between the fibers, and possible global matrix plasticity. Matrix plasticity was observed in the form of slip bands when tested at a slower strain rate ($10^{-5}sec^{-1}$) at 427 °C.

ACKNOWLEDGMENTS

APPENDIX

The constituent properties employed in AGLPLY (ref. 9) are given in this section. Both matrix and fiber were considered isotropic. Fiber properties were independent of temperature except for the coefficient of thermal expansion (CTE).

	Temperature, °C	Modulus of elasticity, E, GPa	Poisson's ratio, ν_{12}	Coefficient of thermal expansion CTE, C^{-1}
Matrix	21	90	[a]0.32	[b]8.1×10^{-6}
	300	80	0.32	9.3×10^{-6}
	550	75	0.32	10.0×10^{-6}
	700	70	0.32	10.5×10^{-6}
Fiber	21	[c]395	[d]0.19	[e]2.2×10^{-6}
	400	395	0.19	2.2×10^{-6}
	700	395	0.19	4.5×10^{-6}

[a]Ref. 12.
[b]Ref. 13.
[c]Ref. 14.
[d]Ref. 15.
[e]Ref. 16.

The matrix moduli were obtained from tensile tests on the unreinforced, laminated, Ti-15-3 matrix, which were run by T.P. Gabb of NASA Lewis. The moduli at 300 °C (572 °F) and 550 °C (1022 °F) were taken from samples that had been given a 24-hr heat treatment at 593 °C (1100 °F) instead of the 700 °C (1292 °F) treatment used in this report. This different heat treatment changed the mechanical properties. For example, the room temperature moduli are 90 and 95 GPa for the 700 and 593 °C heat treatments, respectively. The proportional limits for tests run at 300 and 550 °C (for the 700 °C heat treatment) were calculated by reducing the proportional limits from the specimens heat treated at 593 °C by an amount proportional to the difference in the room temperature moduli of the two heat treatments. The proportional limit (and modulus) at a test temperature of 700 °C for the specimen given a 700 °C heat treatment was estimated from an extrapolation of the proportional limit (and modulus) versus temperature curve.

Matrix proportional limits are given below and represent the adjusted proportional limits. These proportional limits have been reduced by an additional 10 percent to account for the softer region of matrix surrounding the fibers. This was observed in previous work and was suggested to result from chemical inhomogeneities in the matrix as a result of the fibers (ref. 4.) A difference of 10 percent in the matrix hardness was observed between this area and the matrix elsewhere. The proportional limit was adjusted accordingly since the softer matrix occurred adjacent to the fibers - a location where the matrix stresses should be highest and where plastic flow should first occur.

Temperature, °C	Proportional limit, MPa
21	710
300	580
550	450
700	205

A simplified stress-plastic strain curve was used to calculate flow properties of the matrix. These values were taken from a room temperature test of a specimen heat treated at 700 °C and are given below. For high temperatures, the curves were assumed to be identical in shape and only translated to lower stresses by a factor that was equal to the ratio of the proportional limit at that temperature and the proportional limit at room temperature.

Stress, MPa	Plastic strain, percent
710	0
730	0.67
760	1.34
795	2.00

These values reflect the limited strain hardening indicated by the nearly elastic-perfectly plastic behavior observed in tests on the matrix material (ref. 4).

The average residual stresses from cooldown from an assumed stress-free state of 700 °C (1292 °F) to room temperature are given below. In this table, the 1 direction is along the fiber axis, and the 3 direction is perpendicular to the fiber axis. Note that the residual stresses in the $[0°]_8$ and $[90°]_8$ layups are identical; likewise, the $[0°/90°]_{2s}$ and $[\pm45°]_{2s}$ and the $[\pm30°]_{2s}$ and $[\pm60°]_{2s}$. Also, for all fiber architectures, the matrix residual stresses are much below its proportional limit of 710 MPa.

Material	Matrix stresses, MPa			Fiber stresses, MPa		
	σ_{11}	σ_{33}	σ_{13}	σ_{11}	σ_{33}	σ_{13}
$[0°]_8$	275	0	0	-540	0	0
$[0°/90°]_{2s}$ (all plies)	240	135	0	-870	135	0
$[\pm30°]_{2s}$	250	95	55	-775	95	55

REFERENCES

1. B.A. Lerch, D.R. Hull and T.A. Leonhardt, "Microstructure of a SiC/Ti-15-3 Composite," Composites, Vol. 21, No. 3, May 1990, pp. 216-224.

2. J.V. Marzik, "CVD Fibers," Metal and Ceramic Matrix Composite Processing Conference, (Metals and Ceramics Information Center, Columbus, Ohio, USA, 1984).

3. F.E. Wawner, A.Y. Teng and S.R. Nutt, "Microstructural Characterization of SiC (SCS) Filaments," SAMPE Quarterly, Vol. 14, 1983, pp. 39-45.

4. B.A. Lerch, T.P. Gabb and R. A. MacKay, "Heat Treatment Study of the SiC/Ti-15-3 Composite System," NASA TP-2970, 1990.

5. "Standard Test Methods for Tensile Properties for Fiber-Resin Composites," ASTM Standard D3039-76.

6. D.W. Worthem, "Flat Tensile Specimen Design for Advanced Composites," NASA CR-185261, 1990.

7. W.S. Johnson, S.J. Lubowinski and A.L. Highsmith, "Mechanical Characterization of Unnotched SCS/Ti-15-3 Metal Matrix Composites at Room Temperature," Thermal and Mechanical Behavior of Metal Matrix and Ceramic Matrix Composites, ASTM STP 1080, eds. J.M. Kennedy, H. Moeller and W.S. Johnson, 1990, pp. 193-218.

8. R.S. Naik, W.S. Johnson and W.D. Pollock, "Effect of a High Temperature Cycle on the Mechanical Properties of Silicon Carbide/Titanium Metal Matrix Composites," Symposium on High Temperature Composites, American Society of Composites, June 13-15, 1989, Dayton, Ohio.

9. Y.A. Bahei-El-Din and G.J. Dvorak, "Plasticity Analysis of Laminated Composite Plates," ASME Journal of Applied Mechanics, vol. 49, 1982, pp. 740-746.

10. C.A. Bigelow, W.S. Johnson and R.A. Naik, "A Comparison of Various Micromechanics Models for Metal Matrix Composites," Mechanics of Composite Materials and Structures, eds. J.N. Reddy and J.L. Telpy, ASME, 1989, pp. 21-31.

11. L.J. Ghosn and B.A. Lerch, "Optimum Interface Properties for Metal Matrix Composites," NASA TM-102295, 1989.

12. Hertzberg, R.W.: Deformation and Fracture Mechanics of Engineering Materials. John Wiley and Sons, 1976, p. 8.

13. Metallic Materials and Elements for Aerospace Vehicle Structures. MIL-HDBK-5E, pp. 5.121-5.125.

14. Semens, P.A.; Mehan, R.L.; and Moran H.: A Comparison of the Uniaxial Tensile and Pure Bending Strength of SiC Filaments. J. Mater. Sci. Vol. 23, Apr. 1988, pp. 1329-1333.

15. Lang, S.M.: Properties of High Temperature Ceramics and Cermets - Elasticity and Density at Room Temperature. N.B.S. Monograph No. 6, Mar. 1, 1960.

16. Hillmer, N.J.: Thermal Expansion of Chemically Vapor Deposited Silicon Carbide Fibers. Symposium on High Temperature Composites; Proceedings of the American Society for Composites, Technomic Publishing Co., Inc., Lancaster, PA, 1989, pp. 206-213.

TABLE I. - TENSILE DATA FOR 8-PLY SiC/Ti-15-3 COMPOSITE SPECIMENS

[All specimens heat treated at 700 °C for 24 hr unless otherwise noted.]

Laminate code	Specimen number	Initial modulus of elasticity[a], E_T, MPa	Secondary linear modulus of elasticity E_s, MPa	Ultimate tensile strength, UTS, GPa	Failure strain, ε_f percent	Temperature, °C	Strain rate $\dot\varepsilon$ per sec	Fiber volume fraction percent	Vicker's hardness number, H_v	Specimen geometry (b)	Fracture location
[0°]_8	c2	181	NA	----	0.66	21	10^-04	33.9	255.6	A	Grips
	3	192		----	----			34.8	271.9	D	-------
	c4	178		1353	.84			33.6	267.8	A	Midgage
	5	258		1339	.67			34.1	266.0	D	Gage
	6	193		1336	.85			33.6	262.5		Radius
	7	183		1419	1.00			34.0	259.1		Radius
	c8	179		1403	.89			33.4	261.0		Gage
	9	197		1498	.88			35.4	254.1		Midgage
	29	219		1379	.77	427		----	266.0	E	Gage
	30	178		1387	.89	427	10^-03	----	-----	E	
	33	200		1365	.82	427	10^-05	----	-----	E	
	27	170		1432	.96	21	10^-04	----	-----	F	
[90°]_8	43	115	28	293	0.71	427	10^-04	----	-----	E	Gage
	44	115	24	280	0.99	427	10^-05	----	274.3		
	41	130	30	408	1.43	21	10^-04	----	274.4		
	42	119	30	429	1.38	21	10^-04	----	-----		
[90°/0°]_2s	C4	170	121	1060	1.07	21	10^-04	33.1	-----	F	Gage
	C5	103	(d)	999	1.21	21	10^-04	34.8	-----	F	Gage
[0°/90°]_2s	B4	159	113	1029	1.08	21	10^-04	33.2	-----	F	Gage
	B2	148	110	988	1.00	21	10^-04	----	-----	F	Gage
[±30°]_2s	10	150	(d)	----	----	21	10^-04	34.4	266.1	D	------
	11	150		963	1.26			33.7	263.6	D	Gage
	12	152		1004	1.32			34.4	261.1	A	Grips
	13	149		----	----			34.5	269.3	D	-------
	c14	129		963	1.27			34.3	254.5	A	Grips
	c15	142		1001	2.24			34.6	262.6	D	Gage
	c16	141		1039	1.67			34.3	254.0	D	Gage
	18	148		914	1.44			34.2	261.9	D	Radius
	19	150		1054	1.20			33.9	265.7	G	Radius
	22	141		1014	1.04			33.4	273.1	G	Gage
	23	165	81	1000	.99			----	-----	C	Gage
	24	154	83	993	1.50			----	-----	C	Midgage
	25	143	96	999	1.11			----	-----	B	Gage
	26	166	88	1018	1.14			----	-----	B	Gage
[±45°]_2s	A6	93	30	470	7.29	427	10^-04	34.9	274.0	F	Radius
	A11	117	35	530	>4.00	21	10^-04	----	266.3	F	------
	A13	118	28	441	>4.63	427	10^-05	----	293.3	F	------
[±60°]_2s	F1	117	24	390	1.80	21	10^-04	----	-----	F	Gage
	F4	98	21	334	2.95	427	10^-04	----	-----	F	Radius

[a] Sometimes referred to as E11.
[b] See fig. 2.
[c] No heat treatment.
[d] Not recorded.
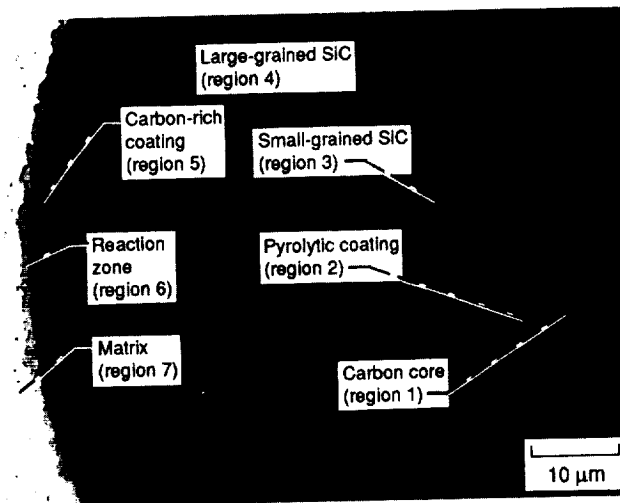
Figure 1.—Cross section of embedded SiC fiber, including fiber-matrix interface.

Specimen geometry	Location			
	a	b	c	d
Straight sided specimens				
A	1.25	10.2	–	–
B	1.90	15.2	–	–
C	2.55	15.2	–	–
Reduced gage section specimens				
D	1.25	10.2	1.85	0.75
E	1.25	14.0	3.80	.80
F	1.25	15.2	3.80	.80
G	2.55	15.2	1.25	1.90
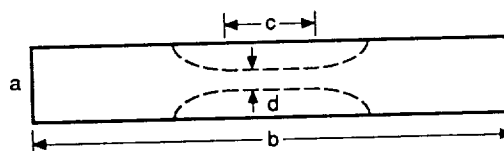
Figure 2.—Tensile specimen geometries. Nominal specimen thickness, 2mm. (Dimensions in centimeters).

P

Face

Edge

Transverse

Ply number
1 2 3 4 5 6 7 8

P

Through-the-thickness

Face
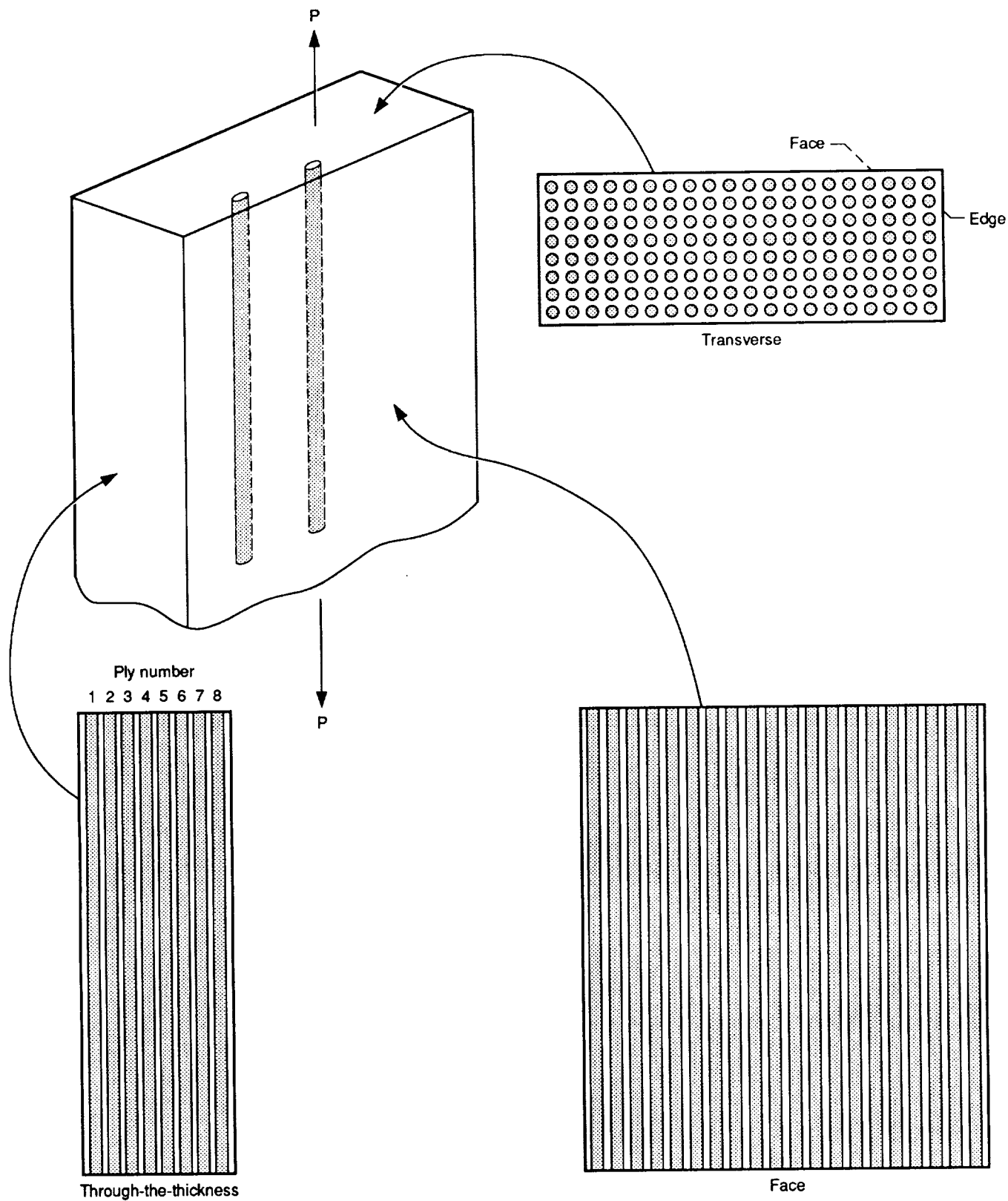
Figure 3.—Orientations of metallographic sections.

23
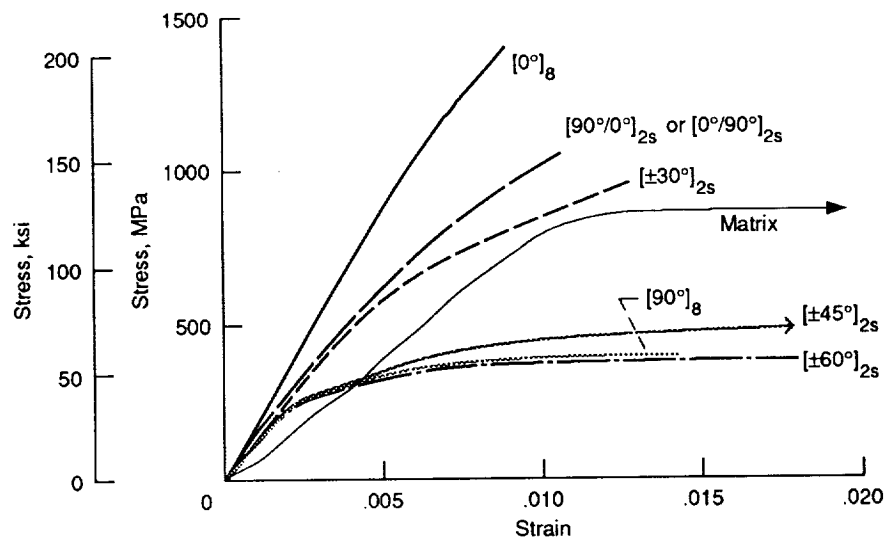
Figure 4.—Room temperature tensile curves for various laminate orientations. Note that the $[\pm 45°]_{2s}$ specimen continues to strains greater than 0.020.

Figure 5.—Anomalously large reaction zone in specimen 5.
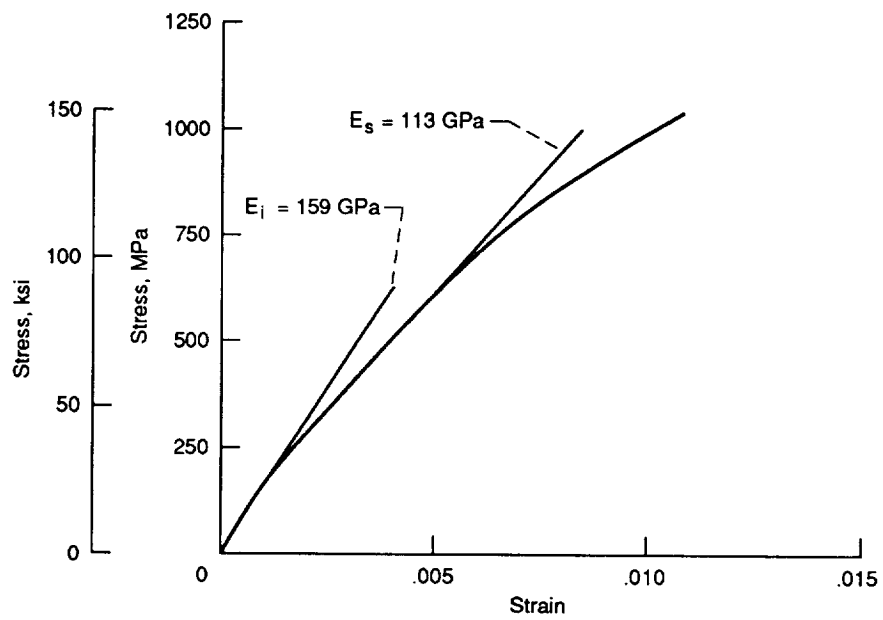
Figure 6.—Tensile curve for $[0°/90°]_{2s}$ specimen. Note the bilinear response at lower strains indicated by tangent lines.
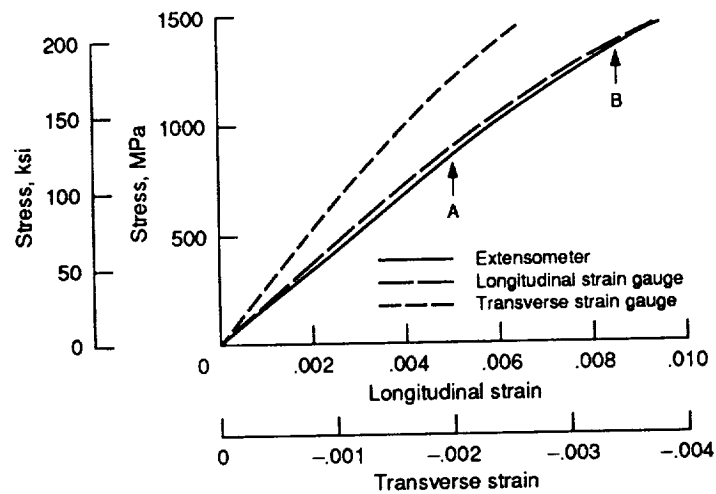
(a) For a [0°]₈ specimen. Points A and B refer to tests that were interrupted at 0.5 and 0.85 percent strain, respectively.
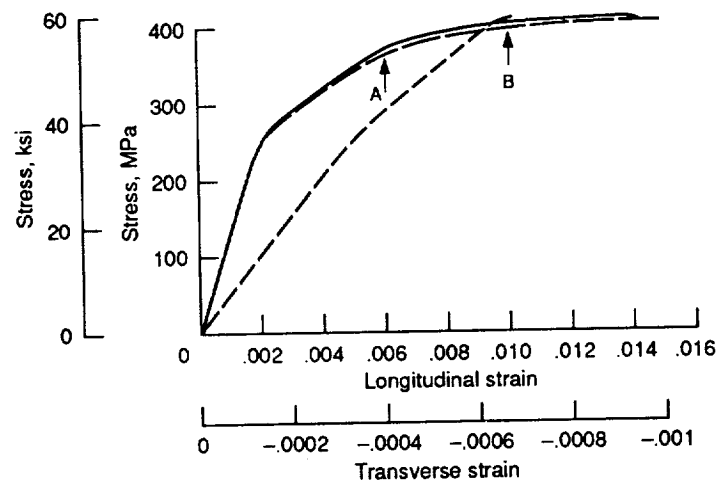
(b) For a [90°]₈ specimen. Points A and B refer to tests that were interrupted at 0.6 and 1.0 percent strain, respectively.
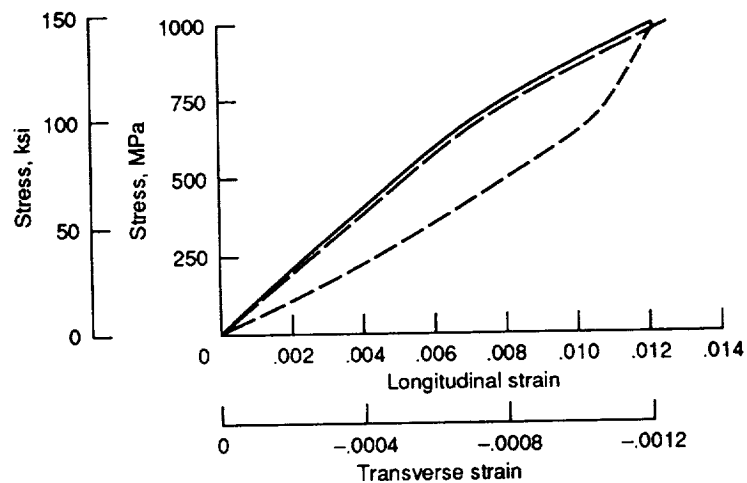
(c) For a [90°/0°]₂ₛ specimen.

Figure 7.—Room temperature tensile curves.

26
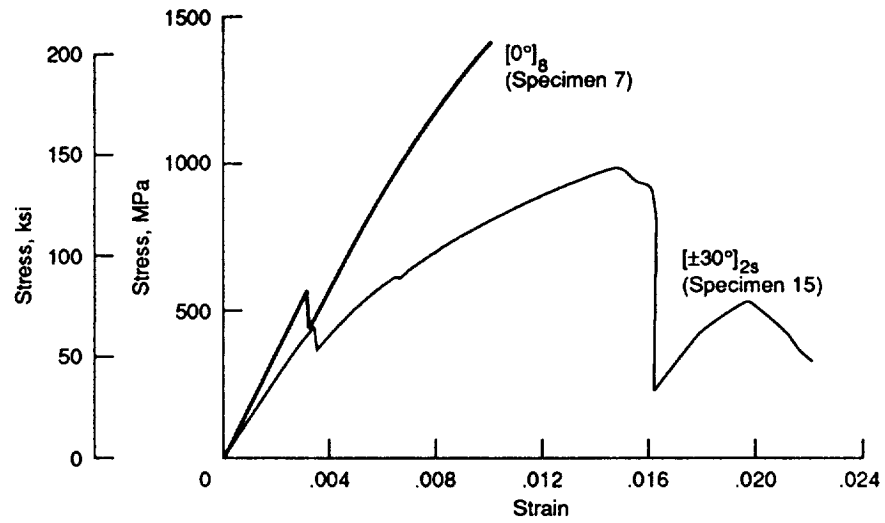
Figure 8.—Room temperature tensile curves showing discontinuities.
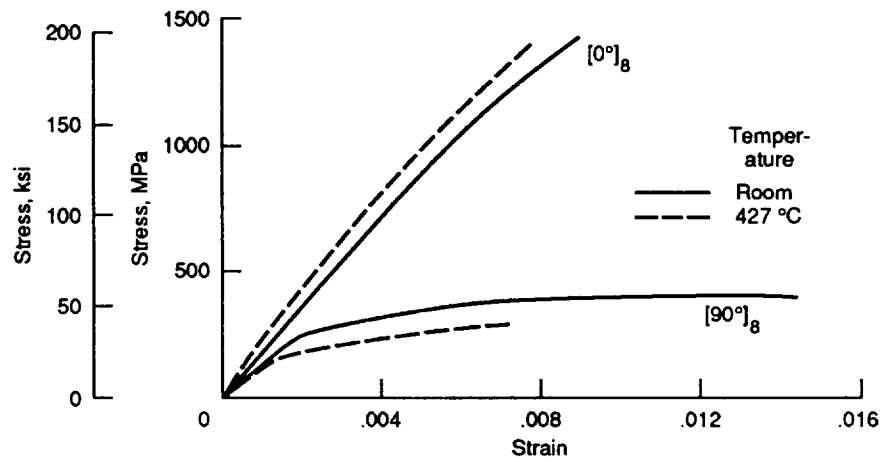
Figure 9.—Tensile curves for $[0°]_8$ and $[90°]_8$. Strain rate, $10^{-4} sec^{-1}$.
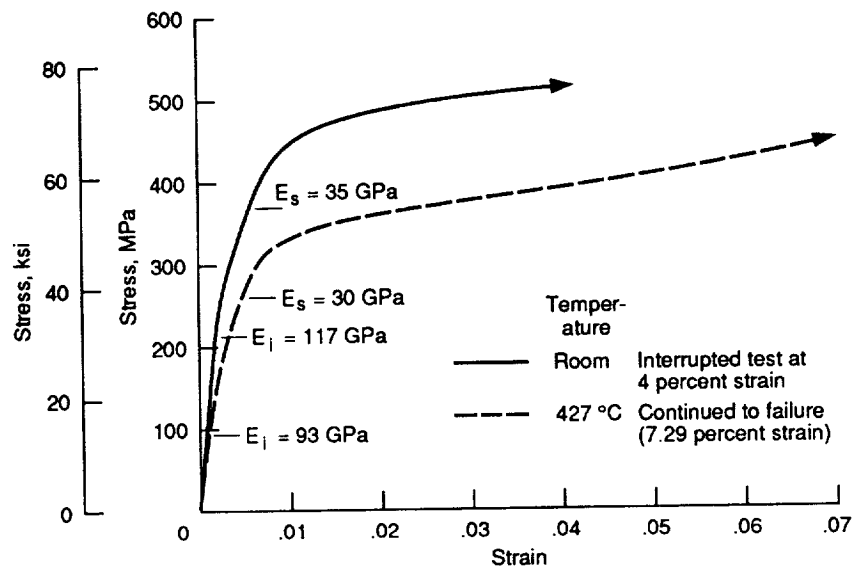
Figure 10.—Tensile curves for $[\pm 45°]_{2s}$. Strain rate, $10^{-4} sec^{-1}$.
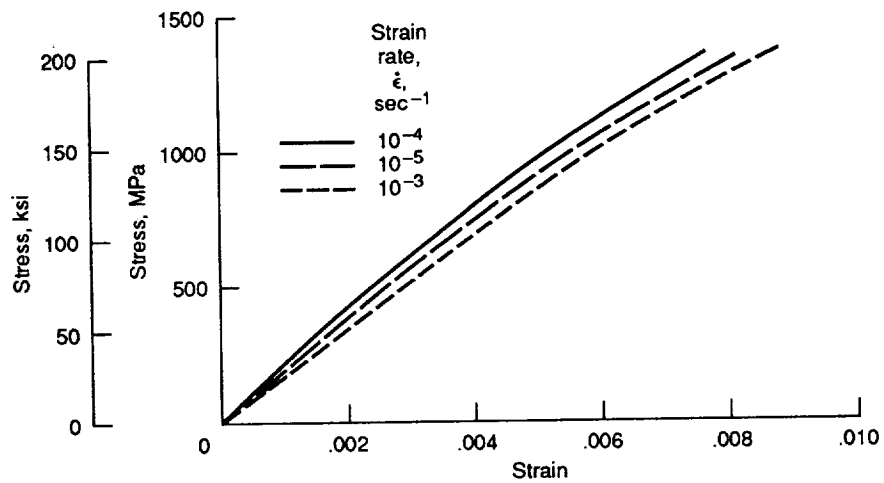
Figure 11.—Tensile curves for $[0°]_8$ specimens tested at 427 °C.
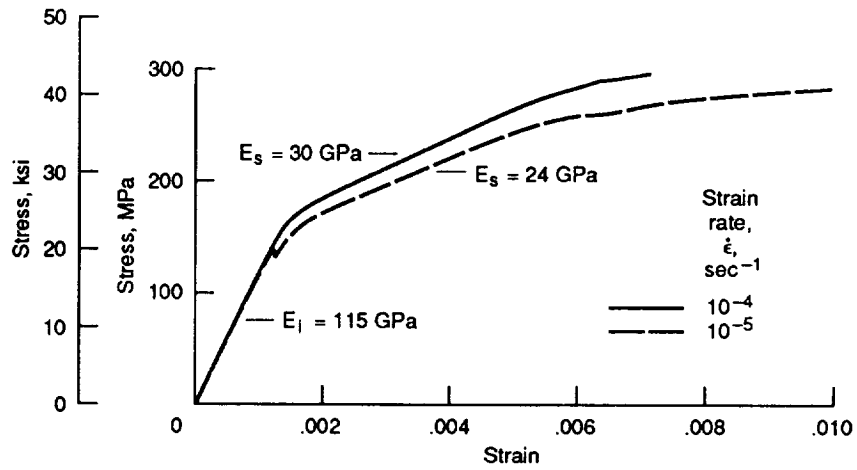
Figure 12.—Tensile curves for [90°]$_8$ specimens tested at 427 °C.
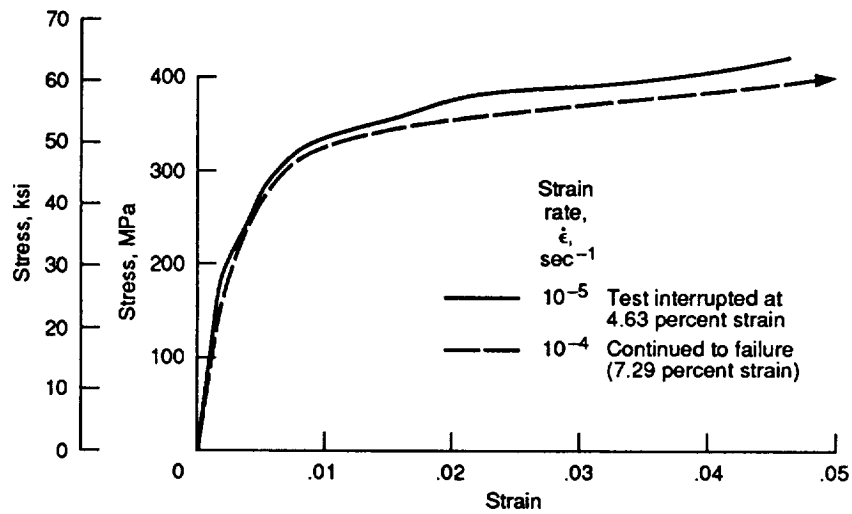
Figure 13.—Tensile curves for [±45°]$_{2s}$ specimens tested at 427 °C.

29

$[0°]_8$ 1 cm

$[\pm 60°]_{2s}$ 1 cm

$[90°]_8$ 1 cm

$[\pm 45°]_{2s}$ 1 cm

$[\pm 30°]_{2s}$ 1 cm

Figure 14.—Tensile specimens showing position and path of main cracks for various layup specimens.

30
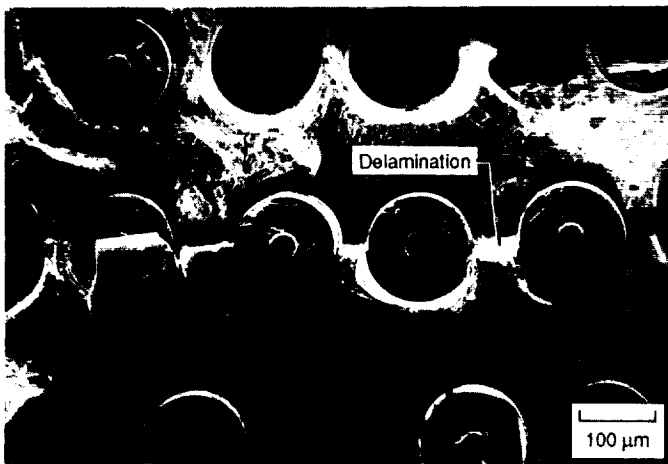
(a) Room temperature test.
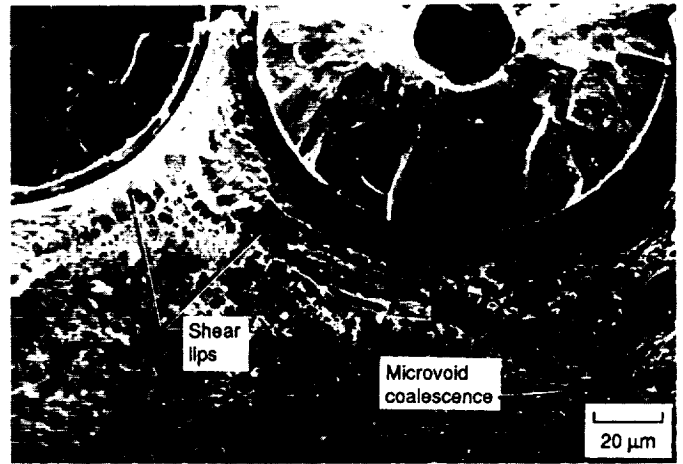
(b) Room temperature test.
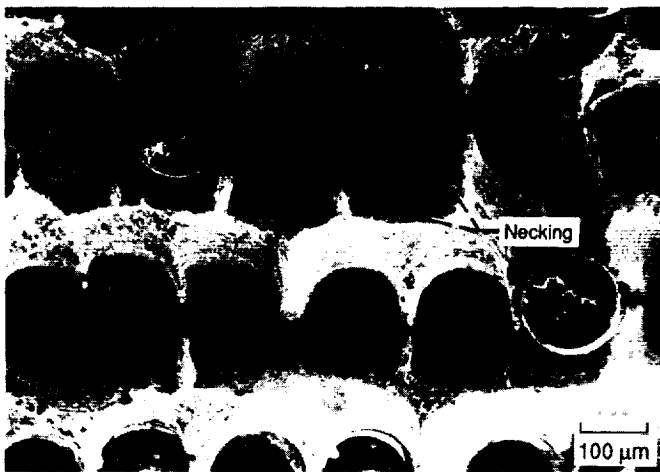
(c) 427 °C test.

ORIGINAL PAGE
BLACK AND WHITE PHOTOGRAPH

Figure 15.—Fractographs of $[0°]_8$ specimens.
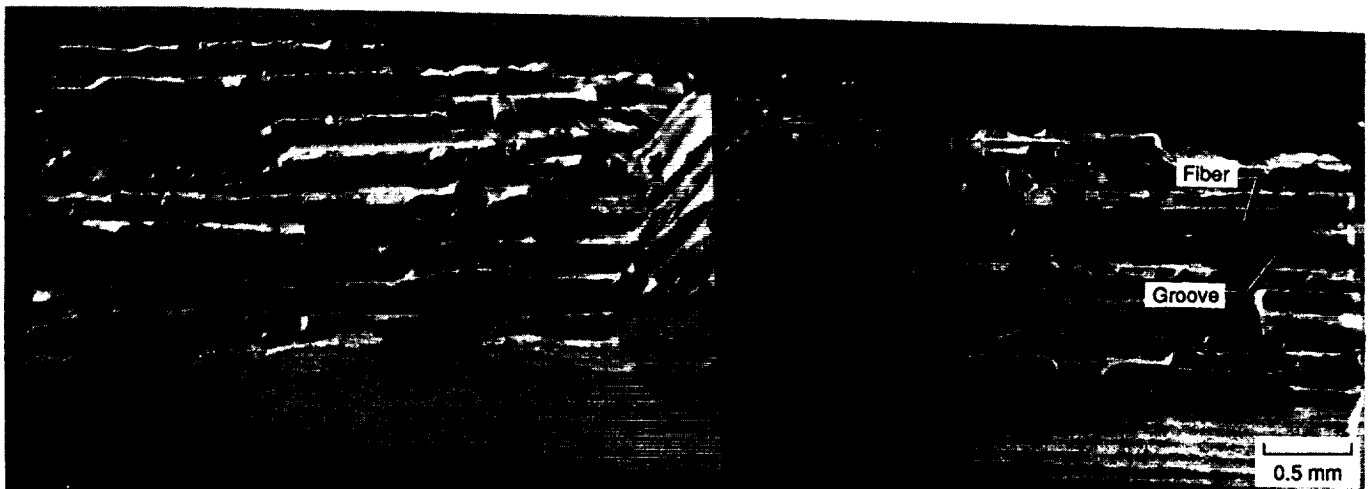
Figure 16.—Fracture surface of $[90°]_8$ specimen tested at 427 °C.

31
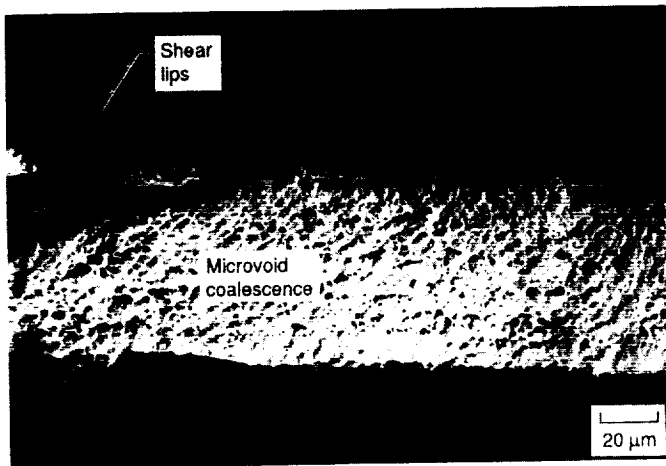
(a) Room temperature test.
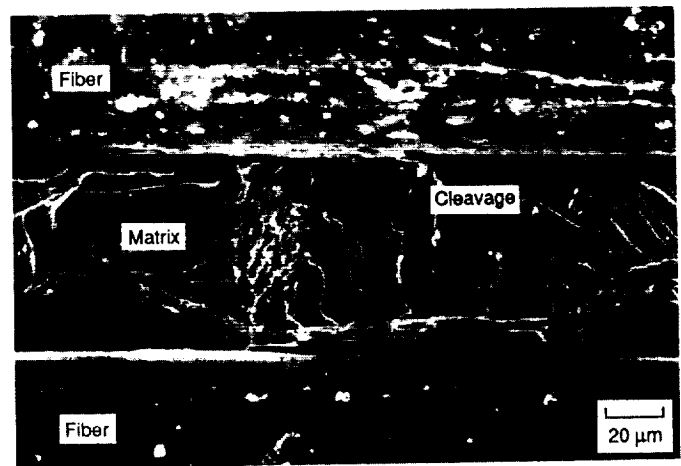
(b) 427 °C test.

Figure 17.—Fractographs of [90°]₈ specimens.

Figure 18.—Fracture surface of [90°/0°]₂ₛ specimen tested at room temperature.
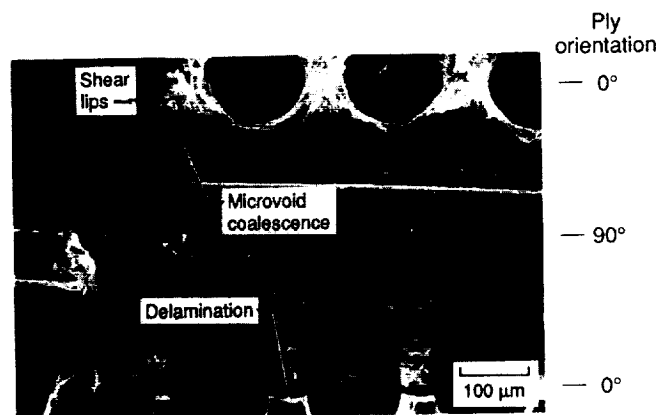
Figure 19.—Fractographs of [90°/0°]₂ₛ specimens tested at room temperature.

32

(a) $[\pm 30°]_{2s}$

(b) $[\pm 45°]_{2s}$

(c) $[\pm 60°]_{2s}$

Figure 20.—Fractographs of crossplied material specimens.

33
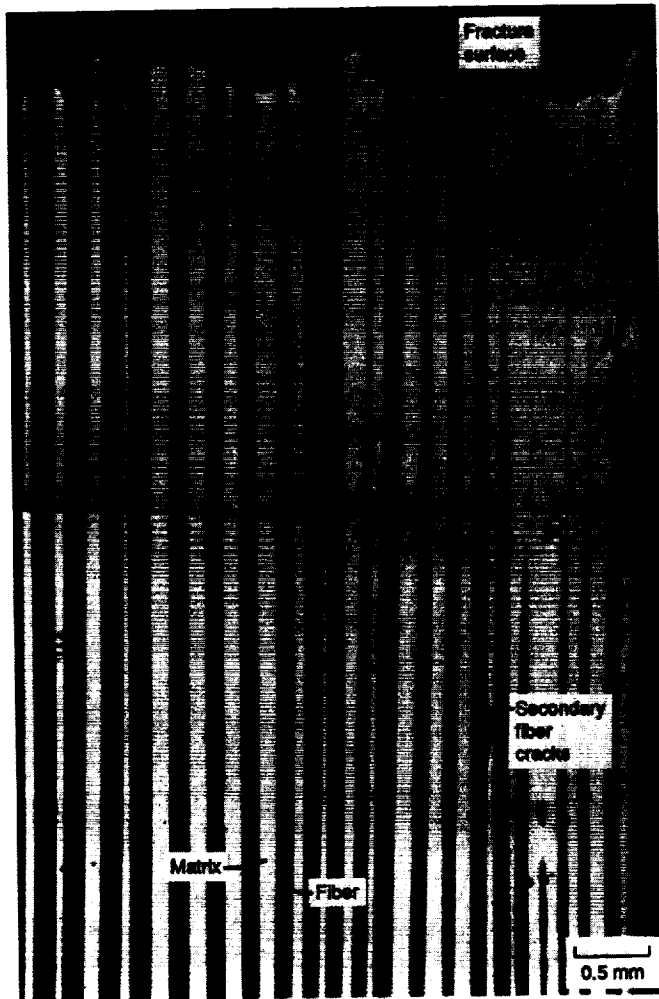
Figure 21.—Face section of second ply of [0°]₈ specimen showing fiber cracks. Specimen tested at room temperature.
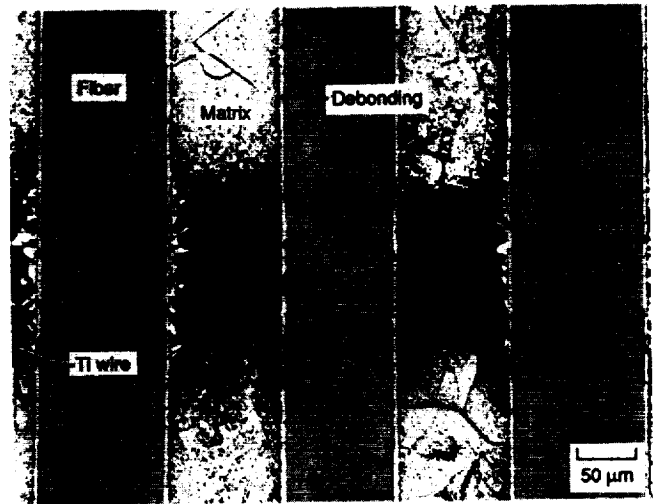
(a) Etched.
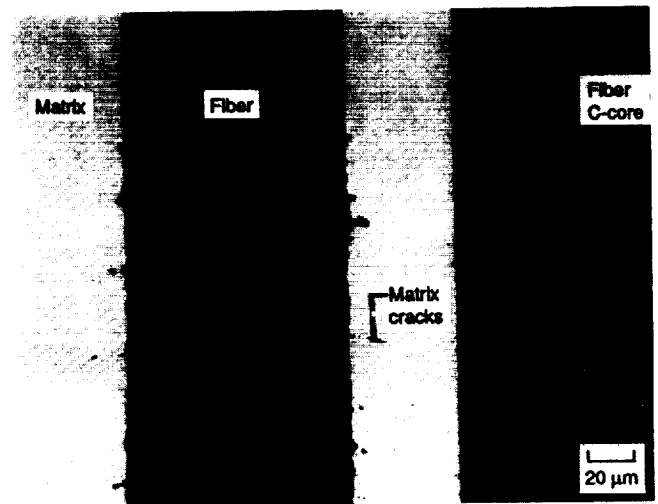
(b) Polished.

Figure 22.—Micrograph of [0°]₈ specimen showing fiber cracks near titanium wire weave. Specimen tested at room temperature.

34

Figure 23.—Face section of [0°]$_8$ specimen tested at 427 °C.
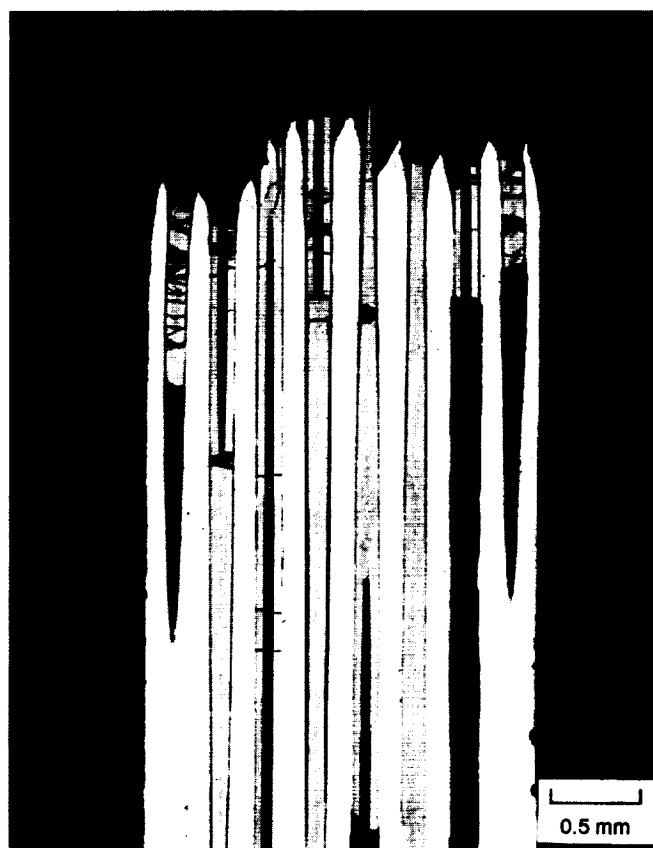
Figure 24.—Through-the-thickness section of [0°]$_8$ specimen showing reduction of area at fracture surface. Specimen tested at 427 °C.
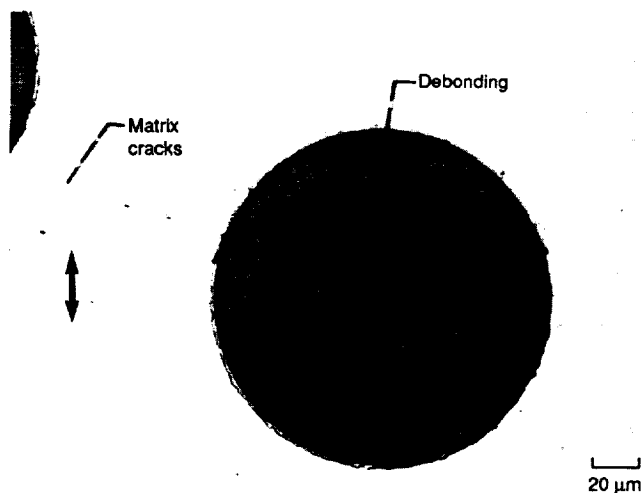
Figure 25.—Through-the-thickness section of [90°]$_8$ specimen showing matrix radial cracks and debonding. Specimen tested at 427 °C. Double pointed arrow indicates loading direction.
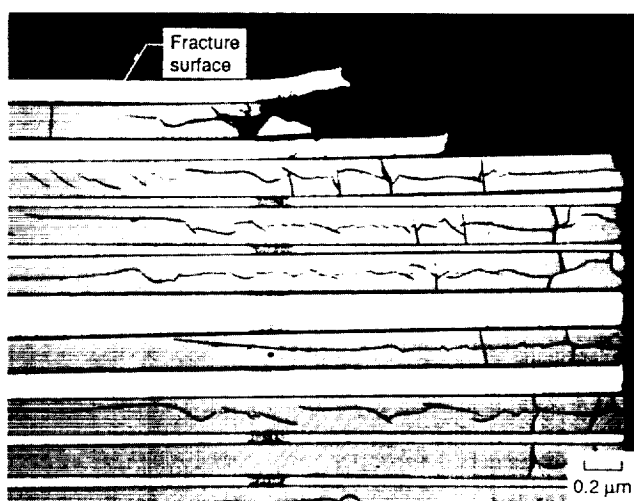
Figure 26.—Face section of [90°]$_8$ specimen tested at room temperature.

35

Figure 27.—Face section of third ply of [0°/90°]$_{2s}$ specimen showing fiber cracks far from fracture surface. Specimen tested at room temperature. Double pointed arrow indicates loading direction.
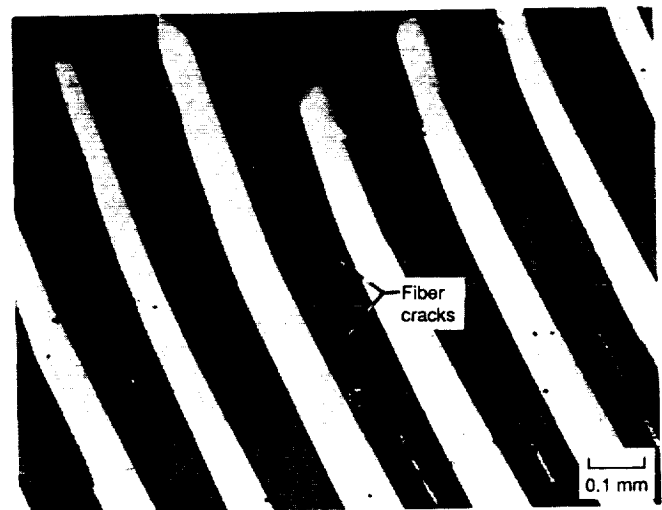
Figure 28.—Face section of [±30°]$_{2s}$ specimen tested at room temperature. Fiber rotation is accommodated by fiber cracking. Double pointed arrow indicates loading direction.
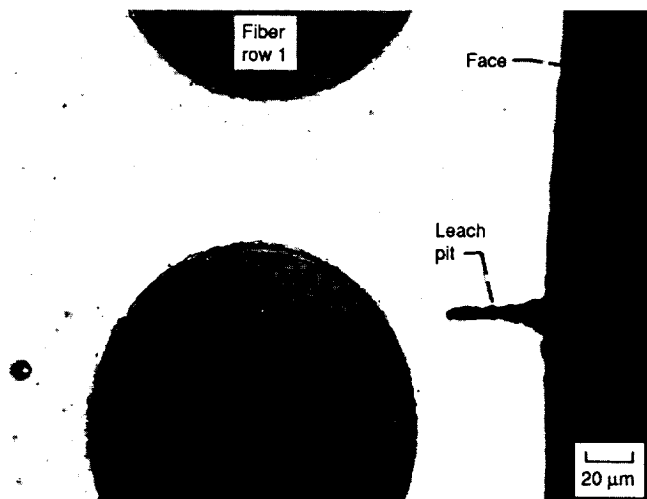
Figure 29.—Through-the-thickness section of $[\pm30°]_{2s}$ specimen showing leach pit created during manufacturing process.
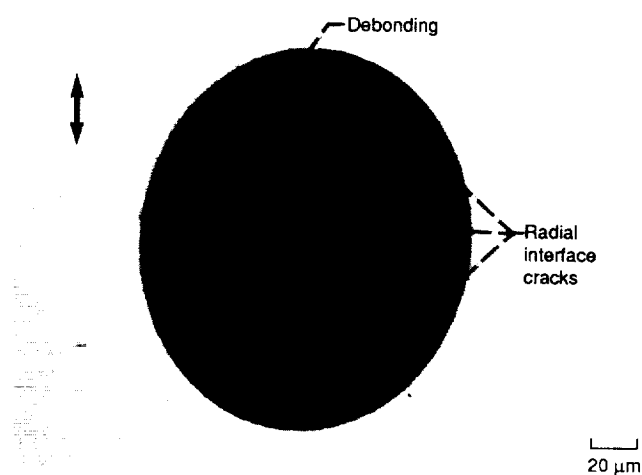
Figure 30.—Through-the-thickness section of $[\pm60°]_{2s}$ specimen showing interface debonding on upper and lower surfaces and radial interface cracks on left and right surfaces. Double pointed arrow indicates loading direction.
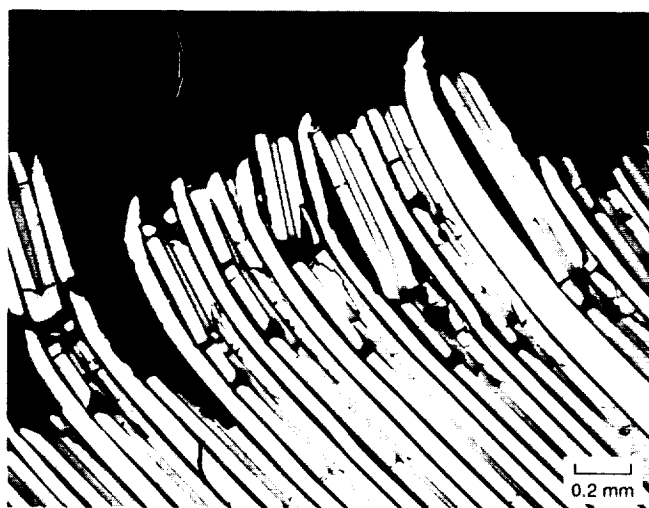
Figure 31.—Face section of $[\pm60°]_{2s}$ specimen showing fracture surface. Specimen tested at room temperature. Double pointed arrow indicates loading direction.
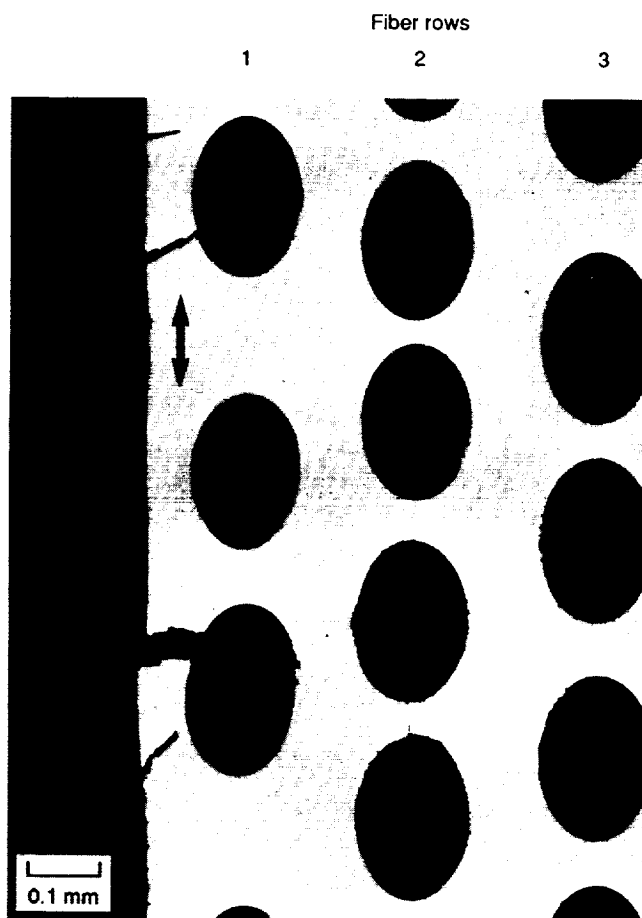
Figure 32.—Through-the-thickness section of $[\pm45°]_{2s}$ specimen. Room temperature test interrupted after 4 percent strain. Double pointed arrow indicates loading direction.
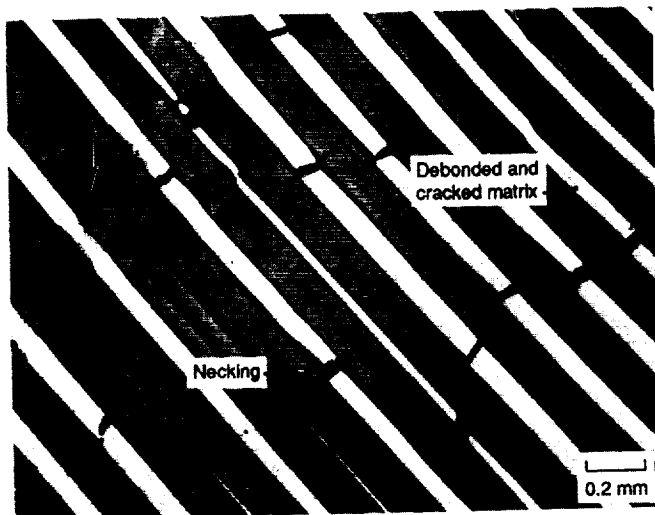
Figure 33.—Face section of $[\pm 45°]_{2s}$ specimen pulled to failure at 427 °C. Double pointed arrow indicates loading direction.
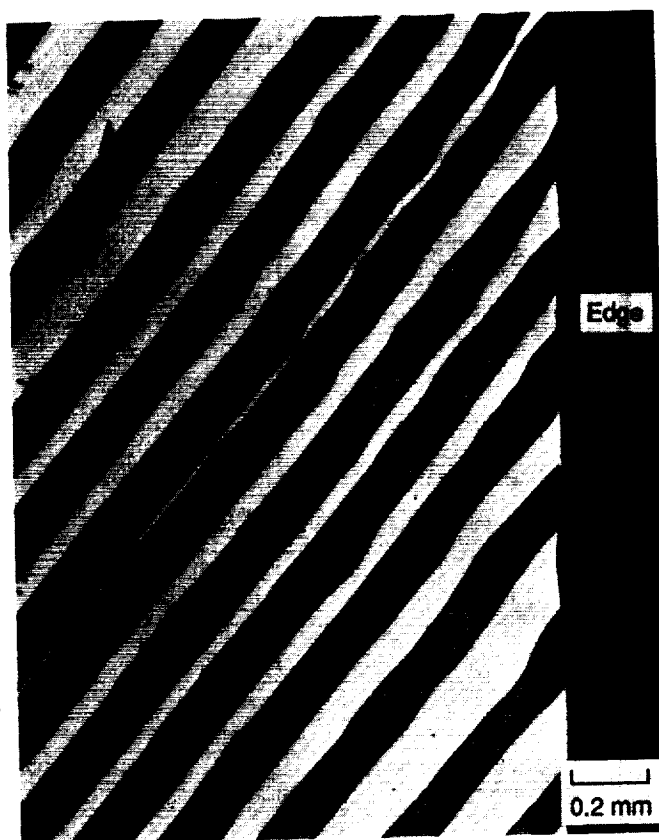
Figure 34.—Face section of $[\pm 45°]_{2s}$ specimen tested to failure at 427 °C. Double pointed arrow indicates loading direction.
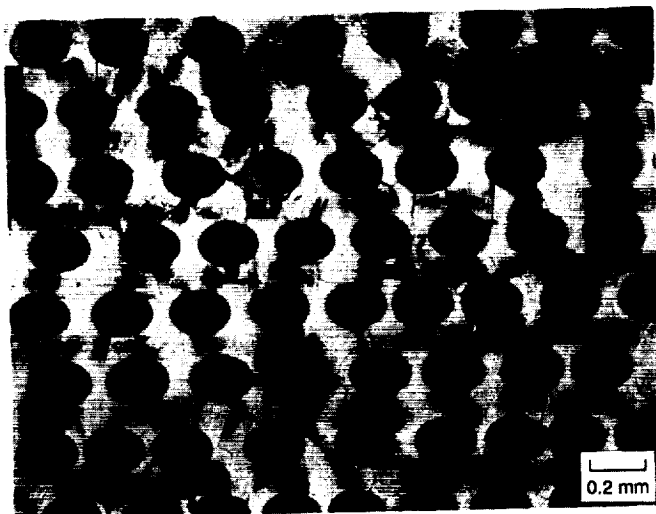
Figure 35.—Sections of $[\pm 45°]_{2s}$ specimen showing slip bands. Test temperature, 427 °C; strain rate, 10^{-5}; etched. Double pointed arrows indicate loading direction.

38
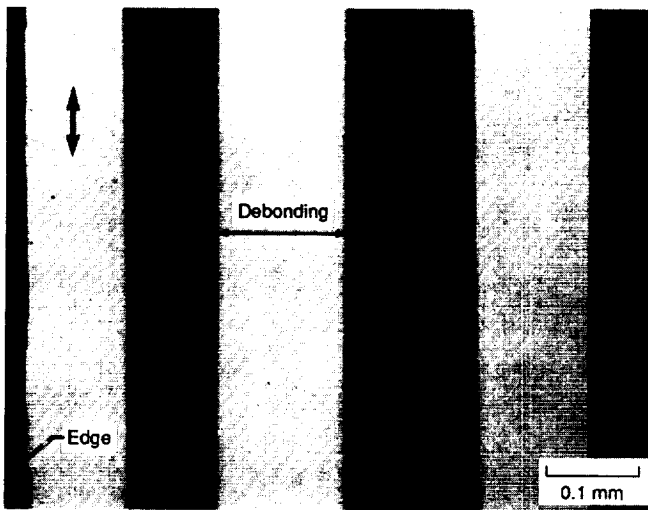
Figure 36.—Face section of $[0°]_8$ specimen tested to a strain of 0.85 percent at room temperature. Double pointed arrow indicates loading direction.
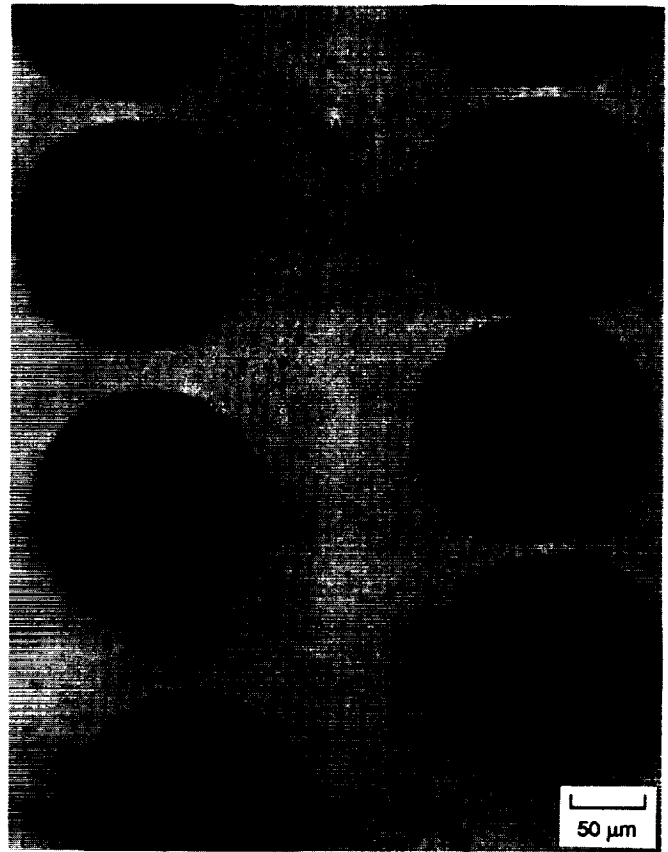
Figure 37.—Through-the-thickness section of $[90°]_8$ specimen showing interface debonding. Specimen tested to strain of 1.0 percent at room temperature. Double pointed arrow indicates loading direction.
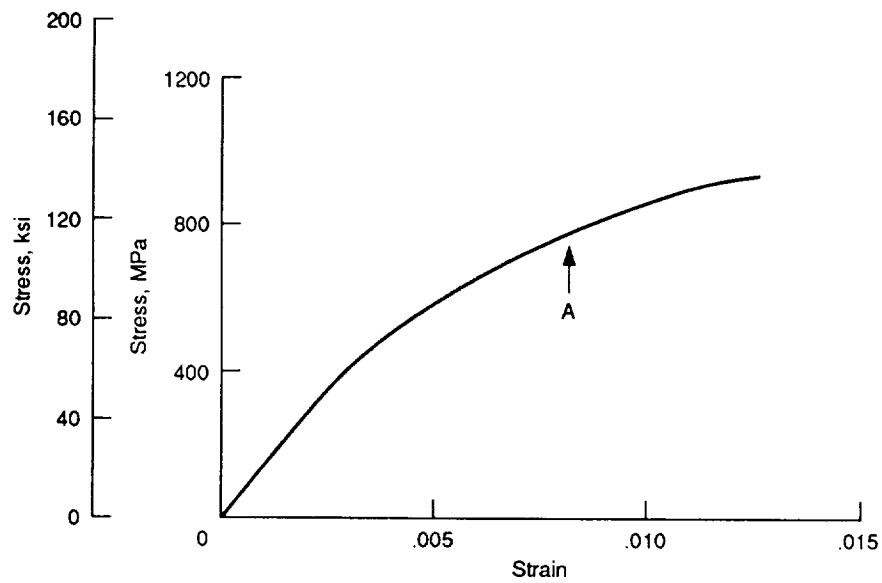
Figure 38.—Room temperature tensile curve for $[\pm30°]_{2s}$ specimen. Point A indicates the interruption of another test at 0.8 percent strain.
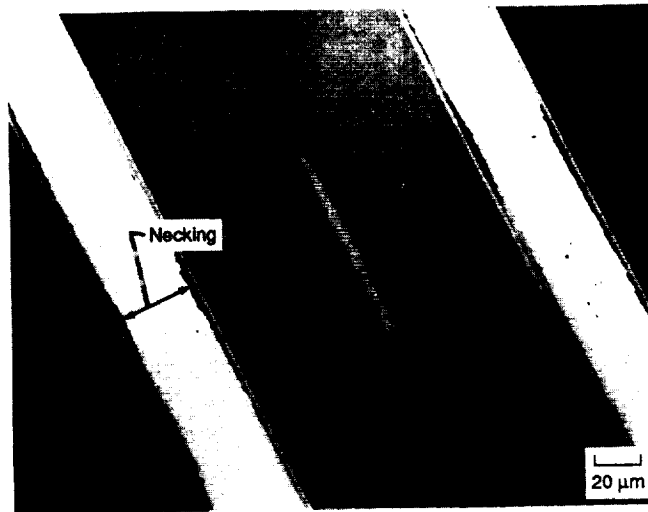
Figure 39.—Face section of $[\pm 30°]_{2s}$ specimen tested at room temperature to a strain of 0.8 percent. Double pointed arrow indicates loading direction.
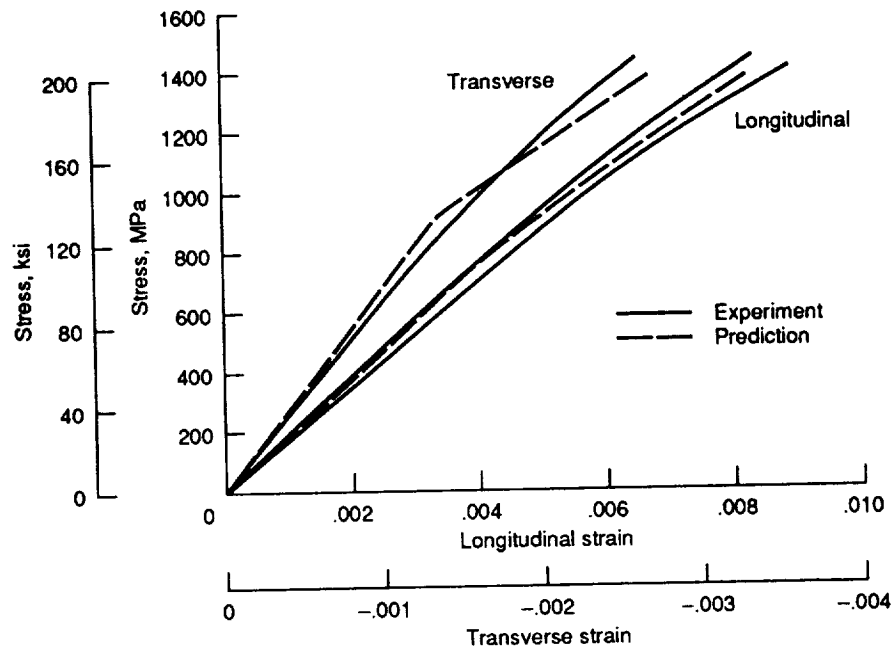
Figure 40.—Room temperature tensile curves for $[0°]_8$ specimens. Data from two specimens are plotted for longitudinal strain.

40
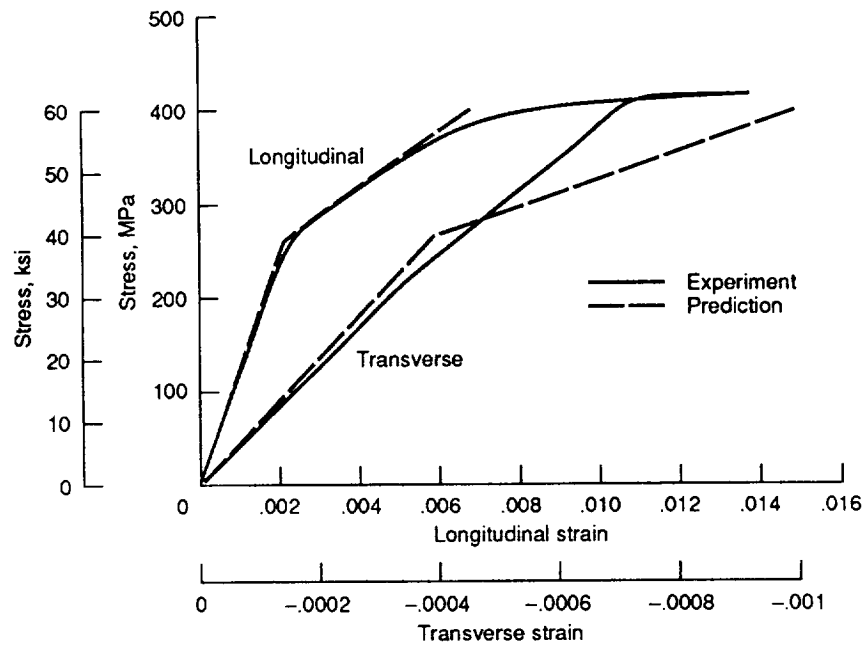
Figure 41.—Room temperature tensile curves for $[90°]_8$ specimen.
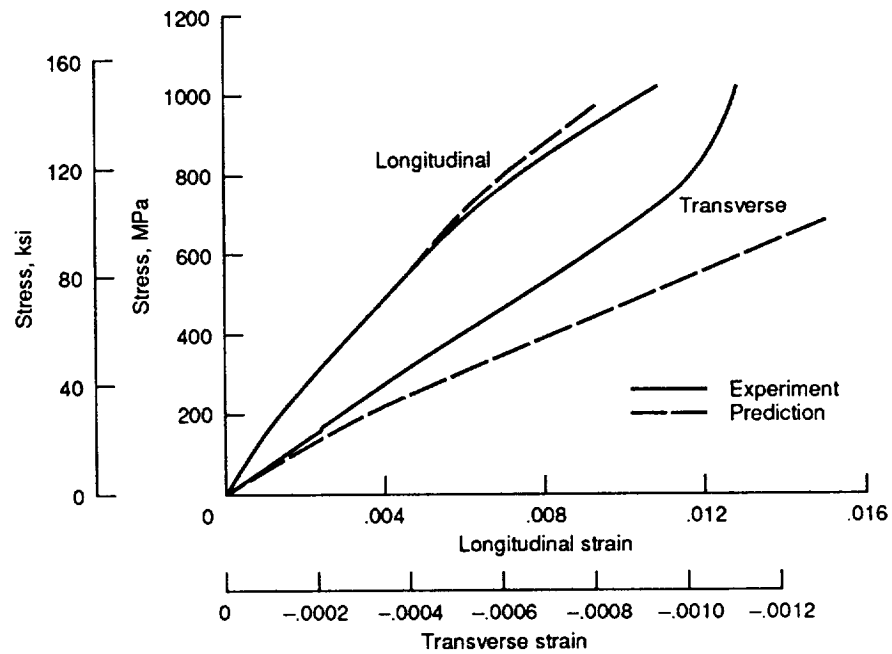
Figure 42.—Room temperature tensile curves for $[0°/90°]_{2s}$ specimen.

41
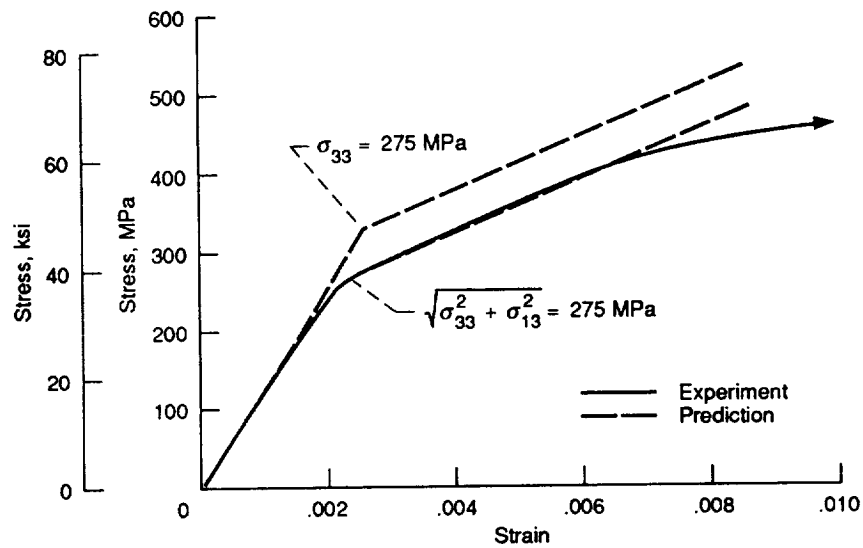
Figure 43.—Room temperature tensile curve for $[\pm 45°]_{2s}$ specimen.

Figure 44.—Room temperature tensile curve for $[\pm 30°]_{2s}$ specimen.

16. Abstract

The damage mechanisms of a laminated, continuous SiC fiber reinforced Ti-15V-3Cr-3Al-3Sn (Ti-15-3) composite were investigated. Specimens consisting of unidirectional as well as cross-ply laminates were pulled in tension to failure at room temperature and 427 °C and subsequently examined metallographically. Selected specimens were interrupted at various strain increments and examined to document the development of damage. When possible, a micromechanical stress analysis was performed to aid in the explanation of the observed damage. The analyses provided average constituent microstresses and laminate stresses and strains. It was found that the damage states were dependent upon the fiber architecture.